Complex Structural Disorder in a Polar Orthorhombic Perovskite Observed Through the Maximum Entropy Method / Rietveld Technique

Alicia María Manjón-Sanz[||,‡,†], *T. Wesley Surta*[||], *Pranab Mandal*[||,¥], *Alex J. Corkett*[||,¶], *Hongjun Niu*[||], *Eiji Nishibori*[‡,§], *Masaki Takata*[‡,£], *John Bleddyn Claridge*[*,||] *and Matthew J. Rosseinsky*[*,||]

[||]Department of Chemistry, University of Liverpool, Liverpool L69 7ZD, United Kingdom

[‡]RIKEN SPring-8 Center, 1-1-1, Kouto, Sayo-cho, Sayo-gun, Hyogo 679-5198, Japan

†Neutron Scattering Division, Oak Ridge National Laboratory, Oak Ridge, Tennessee, 37831 United States

[¥] Department of Physics, SRM University – AP, Mangalagiri, Andhra Pradesh, 522502 India

[¶]Institute of Inorganic Chemistry, RWTH Aachen University, Aachen, Nordrhein-Westfalen, 52056 Germany

[§]Department of Physics, Faculty of Pure and Applied Sciences and Tsukuba Research Center for Energy Materials Science, University of Tsukuba, 1-1-1 Tennodai, Tsukuba, Ibaraki, 305-8577 Japan

[£]International Center of Synchrotron Radiation Innovation Smart (SRIS), Tohoku University, 2-1-1 Katahira, Aoba-ku, Sendai, Miyagi, 980-8577 Japan

ABSTRACT Ambient pressure stable perovskite oxides with all Bi^{3+} on the *A*-site are rare, with only four examples known. Due to the lone pair on Bi^{3+}, these materials are seen as the best alternative to Pb-based piezoelectrics, which are used widely in society. The industry standard piezoelectric, $Pb(Zr_{1-x}Ti_x)O_3$, relies on the [001] polarization of $PbTiO_3$, but there are currently no ambient pressure stable Bi-based perovskites with this polarization vector preventing the creation of an analogous system. We present the full structural analysis of the orthorhombic phase of $(1-x)Bi(Ti_{3/8}Fe_{2/8}Mg_{3/8})O_3$-$xCaTiO_3$, which crystallizes in $Pna2_1$ symmetry with [001] polarization. This symmetry is rare and has only been reported twice for perovskite at ambient conditions. Analysis of maximum entropy method (MEM) models using synchrotron radiation powder X-ray diffraction reveals a disordered *A*-site configuration and the MEM / Rietveld technique generates a structural model of this extreme disorder. Combined Rietveld analysis of X-ray and neutron diffraction data yields accurate description of the local *A*-site configuration, which we use to understand our dielectric, ferroelectric, and piezoelectric measurements. These results give insight in how to stabilize this unique symmetry and inspire new design principles for Bi-based piezoelectrics.

1. INTRODUCTION

The compositional and structural flexibility of perovskite oxides, ABO_3, affords the expression of almost any physical property desired. One area of research which perovskites represent the premiere class of functional materials is piezoelectrics. Lead zirconate titanate ($Pb(Zr_{1-x}Ti_x)O_3$ or PZT) is the commercial standard and has a piezoelectric figure of merit (d_{33}) between 200-600 pC N^{-1}, which is enhanced at the morphotropic phase boundary (MPB, $x \approx 0.48$).[1–3] However, due to the toxicity of Pb^{2+} there is pressure on the scientific community to discover a non-toxic replacement. Bi^{3+} is isoelectronic with Pb^{2+}, giving it a stereochemically active lone pair, but it is non-toxic. Bi^{3+} lone pairs have been shown to control many different properties such as electrical conductivity[4], thermal conductivity[5], thermoelectric properties[6,7], or the non-linear optical response.[8] In piezoelectric, Bi^{3+} is very useful as its stereochemically active lone pair causes asymmetric displacements which break inversion symmetry, making them polar. Simple all Bi *A*-site perovskites such as $BiAlO_3$,[9,10] $BiInO_3$,[11] $BiCoO_3$,[12,13] and materials with complex *B*-sites, such as $Bi(Zn_{1/2}Ti_{1/2})O_3$[14], crystalize in polar, non-centrosymmetric space groups, a requirement for piezoelectricity. Nevertheless, they are only synthetically accessible at high pressure. High pressure synthesis is costly and low throughput; hence these materials will not displace PZT.[15,16] There are four all Bi *A*-site perovskites synthetically accessibly at ambient pressure: $BiFeO_3$,[17–19] $Bi(Ti_{3/8}Fe_{2/8}Mg_{3/8})O_3$ (BTFM),[20] $Bi(Ti_{3/8}Fe_{2/8}Ni_{3/8})O_3$,[20] and $Bi_2(Mn_{4/3}Ni_{2/3})O_6$.[21] Of these four materials, $BiFeO_3$ and BTFM solid solutions have shown the most interest for piezoelectric applications.[22–26]

The crystal chemical design principles employed when searching for new piezoelectrics comes from PZT, where solid solutions of polar endmembers with different polarization directions create an MPB. In the case of PZT, a rhombohedral (R) phase with $[111]_p$ polarization (*R*3*m*,

denoted $R_{[111]}$) becomes tetragonal (T) with $[001]_p$ polarization (*P*4*mm*, denoted $T_{[001]}$) as Ti^{4+} is increased. The MPB is the region in which these different symmetries interface and the d_{33} is enhanced. The exact mechanism within MPB region has been debated for years, and is still a contentious topic.[27] Different models for the long-range (average) structure involve phase coexistence, an intermediate monoclinic (*Cm*), and an adaptive phase model.[28–33] Regardless of the exact mechanism, the electromechanical properties are enhanced as a consequence of the flattened free energy landscape created by the change in polarization direction.[34–39] These principles have been used to create MPBs in many different Pb-free systems such as $(Na_{1/2}Bi_{1/2})TiO_3$-$BaTiO_3$ (NBT-BT),[40,41] $BiFeO_3$-$BaTiO_3$ (BFO-BT),[42,43] and $Bi(Ti_{3/8}Fe_{2/8}Mg_{3/8})O_3$-$BaTiO_3$ (BTFM-BT), all of which have $R_{[111]}$ to $T_{[001]}$ end-members.[24] Recently, the solid solution between BTFM (*R*3*c*, $R_{[111]}$) and orthorhombic, centrosymmetric $CaTiO_3$ (CTO) *(Pnma*) has been shown to have an MPB. In BTFM-*x*CTO, the MPB (*x* = 0.075 - 0.1625) shows a five-fold enhancement in d_{33}, and is unique due to the *Pna*2_1 ($O_{[001]}$) polar, orthorhombic symmetry observed from *x* = 0.175 – 0.40.[26] This [111] to [001] type MPB, with a symmetry that has octahedral rotations along all three crystallographic axes and is generated using a *Pnma* end-member, has not been observed before. The ability to access an orthorhombic symmetry with a $T_{[001]}$ type polarization provides a potential new path for designing Pb-free MPBs, but the chemistry required to access this symmetry is unknown.

Pna2_1 symmetry is uncommon in perovskites. This symmetry has been observed in perovskites synthesized at high pressure, such as $BiInO_3$[11] and $Bi(Ni_{1/2}Ti_{1/2})O_3$,[44] or at low temperature, seen in $CdTiO_3$[45–47] and $TbMnO_3$.[48] Reports on ambient temperature and pressure $Bi_{0.8}Gd_{0.2}FeO_3$,[49] and $Bi_{0.7}La_{0.3}FeO_3$[50] have claimed *Pna*2_1 symmetry, but do not support these claims using multiple corroborating measurements. The polarity of $Bi_{0.8}Gd_{0.2}FeO_3$ is observed by

piezoresponse force microscopy studies, but Rietveld analysis against laboratory powder X-ray diffraction (PXRD) data were not able to discriminate between *Pnma* and $Pna2_1$ space groups.[49] Dielectric and dilatometry measurements indicated that $Bi_{0.7}La_{0.3}FeO_3$ has a phase transition, with indexing and Rietveld analysis of laboratory PXRD data concluded that $Bi_{0.7}La_{0.3}FeO_3$ has a $Pna2_1(00\gamma)s000$ superstructure.[50] In BTFM-*x*CTO, $Pna2_1$ symmetry is confirmed using ferroelectric, piezoelectric, dielectric, and second harmonic generation (SHG) measurements in combination with synchrotron radiation powder X-ray diffraction (SR-PXRD) and electron diffraction.[26] The clear confirmation of $Pna2_1$ symmetry has prompted us to investigate the structure of this rare and hard to access $O_{[001]}$ phase in order to better understand how it is stabilized. We analyze the $O_{[001]}$ phase of BTFM-*x*CTO using the maximum entropy method (MEM) and the MEM/Rietveld method against SR-PXRD data. The resulting model is then used in a combined Rietveld refinement against SR-PXRD and neutron powder diffraction (NPD) data to yield a detailed structural description which requires three different *A*-site positions. We present the first structural report of this polar $O_{[001]}$ phase, detail the interesting disorder observed, and discuss the chemical and structural implications for the ferroelectric, piezoelectric, and dielectric properties.

2. EXPERIMENTAL SECTION

2.1. Synthesis. Samples of BTFM-*x*CTO in the range $0.175 \leq x \leq 0.40$ were synthesized by standard solid state synthesis methods as has been described previously.[26]

2.2. Pellet processing. For physical properties measurements pellet samples of composition $x = 0.20$ were prepared by the previously reported processing protocol.[26]

2.3. Compositional analysis. Electron diffraction experiments (selected area electron diffraction and convergent beam electron diffraction (CBED)) were conducted using a JEOL 2000FX electron microscope operating at 200 kV for compositions x = 0.175 and 0.20, as described in our previous paper.[26] Energy dispersive X-ray spectroscopy (EDX) data were also collected with the same microscope. EDX analysis of 10 grains were examined to determine homogeneity. EDX correction factors, for the different elements, were estimated by measuring the EDX spectra of appropriate standards. The purity of the standards was confirmed using X-ray diffraction.

2.4. Diffraction Experiments. SR-PXRD data were collected for BTFM-xCTO when x = 0.175, and 0.20 on the powder diffraction beam line BL44B2 at SPring-8.[51] The diffractometer is equipped with a large Debye-Scherrer camera with an imaging plate (IP) detector. A CeO2 standard powder sample (NIST) was used for wavelength calibration. The powder sample of x = 0.175 was loaded into a 0.1 mm diameter Lindemann glass capillary, and normal and high counting statistics data were measured over a 2θ range from 2° to 75° every 0.01° at a temperature (T) of -173 °C. The calibrated wavelength of the incident X-ray was 0.50025 Å. A slit mask with a width of 10 mm was inserted in front of the detector. For the measurement of very weak reflections a silver film was inserted in front of the detector to reduce the background scattering, including X-ray fluorescence from transition metals, as much as possible. Furthermore, a lead sheet was attached to the detector at a particular 2θ region to avoid measuring the main peaks of the perovskite structure and not saturate the IP. For variable temperature (VT) SR-PXRD experiments on x = 0.175, data were collected in the temperature range from -173 to 27 every 50 °C for 5 min. For VT SR-PXRD experiments on x = 0.20, the sample was loaded into a 0.2 mm diameter Lindemann glass capillary. Data were collected in the temperature range from -173 to 27 °C every 25 °C for 3 min. The wavelength of the incident X-ray used was 0.49995 Å. Data were measured

over a 2θ range from 0.01° to 78.02° every 0.01°. Data were also collected in the temperature range from 27 to 357 °C every 30 °C for 5 min. The wavelength of the incident X-ray used was 0.450179(8) Å. Data were measured over a 2θ range from 0.01° to 78.02° every 0.01°.

NPD data were collected for x = 0.175 and 0.20 on the High Resolution Powder Diffractometer (HRPD) (ISIS, U.K.) at room temperature. Approximately 7 g of the materials were loaded into 10 mm diameter vanadium cans and data were measured using the highest-resolution back-scattering bank 1 ($160° < 2\theta < 176°$), the 90° bank 2 ($80° < 2\theta < 100°$), and the low-angle bank 3 ($28° < 2\theta < 32°$). For structural analysis, NPD data collected on banks 1 and 2 were used. All data were corrected for absorption before Rietveld analysis.

The SR-PXRD data for x = 0.175 collected at T = -173 °C were indexed using the program DICVOLB6.[52] The first thirty peaks of the powder pattern in the data range from 3.00 to 28.60° were evaluated. Le Bail analysis and Rietveld refinements using SR-PXRD data were performed using the Synchrotron Powder (SP) software developed by the Sakata laboratory.[53] For Le Bail analysis performed on x = 0.175 at T = -173 °C for the space group assignment, a 2θ range from 3 to 40° was analyzed. A split pseudo-Voigt profile function was used, and the background was modelled manually. This SP software allows simultaneous refinement of two different sets of powder diffraction data collected at BL44-B2 and yields outputs of the observed structure factors. These outputs obtained were directly used as input data for further MEM[54] analysis. The MEM analysis was carried out using the program ENIGMA.[55] Le Bail fits for the VT SR-PXRD data on x = 0.175 and 0.20 were performed using the 2θ range from 3 to 41°.

Combined Rietveld Analysis on SR-PXRD and NPD data for x = 0.175, and 0.20 were performed using Topas Academic.[56] The background was fit with a Chebyshev polynomial with

12 terms to fit SR-PXRD data, and 9 terms to fit each NPD data set. The atomic positions of atoms on the same sites were set to be the same value. All occupancies were set to match the stoichiometry of the desired composition. The background, lattice parameters, profile parameters, scale factor, atomic positions, atomic displacement parameters were all refined during analysis.

2.5. Physical Properties Measurements. Pellet samples for dielectric measurements were polished to a thickness of 0.1-0.3 mm with 20 micron SiC foil using a Struers Tegramin-30 semi-automatic polishing machine, and electroded with Pt paint or sputtered gold. The Pt paint was cured at 850 °C for 30 min. High temperature dielectric measurements were performed using an Agilent E4980 LCR meter using a custom sample holder and a program created in LABVIEW.[57] For the dielectric measurements performed on poled pellets, the poling procedure used was as follows: discs were first heated up from room temperature to 150 °C using a heating rate of 5 °C min-1. Then, an electric field of 100 kV cm-1 was applied and held for 15 minutes. Afterwards, the temperature was decreased from 150 °C to room temperature using a cooling rate of 1 °C min, while still applying the electric field. Finally, the electric field was removed at room temperature.

Pellet samples for polarization versus electric field ($P(E)$), strain versus electric field ($S(E)$), and positive up negative down (PUND) measurements were polished with 20, 15, and 5 micron SiC foils resulting in a mirror surface, and a thickness of ~ 0.15 mm. Resulting pellets were electroded with either silver paste for $P(E)$ and $S(E)$ measurements or sputtered with gold for direct piezoelectric measurements. An aixPES (aixACCT GmbH, Germany) was used to perform $P(E)$, $S(E)$ and PUND measurements at room temperature and at higher temperatures. Samples were measured while submerged in silicone oil in order to avoid electrical breakdown.

3. RESULTS AND DISCUSSION

3.1. *3.1.1. Compositional analysis on x = 0.175 and 0.20.* EDX data were already published in our previous paper and match with the expected compositions. [26] Figure S1 shows, the EDX data for x = 0.175 and 0.20.

3.2. Structural Analysis. *3.2.1. Indexing and space group assignment on x = 0.175.* As we previously published, the SR-PXRD data for $x \geq 0.175$ were indexed to an orthorhombic unit cell. SHG measurements show that all these materials are polar, indicating a non-centrosymmetric structure.[26] The non-polar end member of the solid solution CTO, which crystallizes in the centrosymmetric space group *Pnma*, gave no SHG response as expected.[46] More specifically, we reported that the space group for x = 0.20 is the polar orthorhombic $Pna2_1$ (a subgroup of *Pnma*) using CBED.[26]

In this work, we corroborate the space group assignment for orthorhombic compositions to $Pna2_1$ based on the reflection conditions using high quality SR-PXRD data. The composition x = 0.175 was initially selected for indexing, space group assignment, and structural analysis. This selection is because the peaks for x = 0.175 are sharper than for x > 0.175 (Figure S2a) suggesting a single phase material. Furthermore, it does not show any Aurivillius ($Bi_5FeTi_3O_{12}$) or Sillenite ($Bi_{25}FeO_{40}$) impurities (Figure S2b). These two facts made the indexing process easier to perform on x = 0.175 than when x > 0.175. The lattice constants determined from indexing are: a = 7.866(3) Å, b = 5.5920(8) Å, and c = 5.5657(10) Å for x = 0.175 at a temperature (T) of -173 °C. Data at this temperature were selected to be studied, because the atomic displacement of the atoms at low temperatures is smaller as thermal motion is decreased, allowing better atoms to be located more easily. The decreased thermal motion also leads to increased signal to noise, allowing reflections with low intensity to be more easily observed, particularly in the high angle region.

3.2.2. Le Bail analysis on x = 0.175. Le Bail analysis were performed for data collected at T = -173 °C in the three polar subgroups of *Pnma*: *Pna*2_1 (33), *Pmc*2_1 (26), and *Pmn*2_1 (31), in the six possible different settings for an orthorhombic structure (*abc*, *acb*, *bac*, *bca*, *cab*, and *cba*). The lattice constants obtained from indexing were used for the analysis and were not refined. Enlargements of Le Bail fits for x = 0.175 at T = -173 °C are shown in the six different lattice settings for *Pna*2_1 (Figures S3-8), *Pmc*2_1 (Figures S9-14), and *Pmn*2_1 (Figures S15-20) in the SI. The quality of the Le Bail fits results was examined, and their reflection conditions carefully investigated. Table S1 summarizes the results of these Le Bail fits and compares: fit quality parameter (R_{wp}), number of total reflections, number of reflections in the model with no corresponding peak in the data, and number of missing reflections in the model with corresponding peak in the data for the 2θ range from 4.8 to 20°. Upon inspection of all the Le Bail fits (Figures S3-20), we observe that the Le Bail fit in *Pna*2_1, lattice setting *bca*, (Figure S6) fits very well with an R_{wp} = 2.15%, and accounts perfectly for all observed reflections in SR-PXRD data. Furthermore, there are neither extra reflections in the structural model not needed to fit the observed data, nor missing reflections needed to fit the observed data. For Le Bail fits in the other lattice settings of *Pna*2_1 (Figures S3-5, S7-8), and all the lattice settings in *Pmc*2_1 (Figures S9-14), and *Pmn*2_1 (Figures S15-20), either extra reflections in the structural model not needed to fit the observed data, and/or missing reflections needed to fit the observed data appear, as indicated by black boxes. Therefore, we can uniquely assign the space group *Pna*2_1 in the lattice setting *bca*.

3.2.3. MEM / Rietveld analysis against SR-PXRD data on x = 0.175. Rietveld refinements on SR-PXRD in *Pna*2_1 symmetry with the *bca* lattice setting were performed on x = 0.175 at room temperature. The initial structural model with single *A* and *B*-sites, and unsplit O fits the data well visually and accounts for all of the low angle reflections, matching the intensities and peak shapes,

and yielding an R_{wp} = 3.94%. However, at angles greater than 32° the model does not account for SR-PXRD peak intensities appropriately (Figure S21). The model has large isotropic atomic displacement parameters (B_{eq}) on the *A*-site (3.88(4) Å^2) and the O1 site (6.0(14) Å^2). Large *A*-site B_{eq} values are common in perovskites with cation disorder such as $Pb(Mg_{1/3}Nb_{2/3})O_3$, $Pb(Sc_{1/2}Nb_{1/2})O_3$, or $(K_{1/2}Bi_{1/2})(Sc_{1/2}Nb_{1/2})O_3$, which have *A*-site B_{eq} values of 4, 2.5, and 4.6 Å^2, respectively.[58–60] Also, the related material BTFM-BT[24] shows a large *A*-site B_{eq} value of 7.30 Å^2. All of the refined parameters are reported in Table S2. Due to the large atomic displacement parameters on the *A*-site and poor fit to SR-PXRD at high angle, the electron density distribution was investigated for x = 0.175 at T = -173 °C by Fourier difference analysis. As Figure S22 shows, there is electron density mismatch on all sites and does not reveal a clear origin of the high angle peak intensity mismatch in the SR-PXRD. Therefore, the electron density distribution was further investigated by MEM to identify the discrepancy between the structural model and the observed data.[54] MEM enhances the extraction of accurate structural information using SR-PXRD data, and this method is very effective for creating structural images at the electron density level. The study of Bi^{3+} inert pair effects with MEM have been demonstrated in a variety of materials such as charge ice pyrochlores[61] and Aurivillius ferroelectrics.[62]

Based on the SR-PXRD data, and the initial model for the x = 0.175 material, the observed and simulated electron density maps were obtained by MEM. In the calculation, the unit cell was divided into 64 x 64 x 96 pixels. The pixels were determined by the considerations of lattice constants, space group symmetry and asymmetric unit of the unit cell. The charge density by MEM is affected by the reciprocal resolution of the data, uncertainties of structure factors (F), stopping criteria, and Lagrange multiplier of the analysis. To avoid these effects as much as possible, at first, we did MEM analysis using the calculated structure factors with uncertainties based on the

statistical uncertainties of Bragg intensities. The stopping criteria of the analysis was the same as for the original report on MEM analysis of SR-PXRD data.[54] We optimize the data resolution, Lagrange multiplier and stopping criteria using this analysis. We used the fixed Lagrange multiplier to avoid unexpected results. The reciprocal resolution was determined as 0.5 Å. The Lagrange multiplier was fixed to 0.1. The stopping criteria for the calculated structure factors was the same as for the original MEM report. The typical iteration consisted of 100 cycles. Two kinds of stopping criteria were used for the observed structure factors. One was three times the number of iteration cycles of that of calculated structure factors. Another was the same as for the original MEM paper. In the early stage of analysis, we used the former condition to avoid overfitting the data. We were able to use the later condition when the reliability factor of the Rietveld analysis was sufficiently small. The initial model constructed based on MEM map was confirmed not only by the Rietveld refinement of SR-PXRD data but also by the refinement of NPD data. The structural model and the corresponding 3D electron density distribution from MEM analysis on SR-PXRD data can be seen in Figures 1a and b, respectively. The electron density distribution map shows that the *B*-sites and oxygens are well accounted for, but the electron density associated with the *A*-site is large and anisotropically distributed. In Figure 1c, the observed electron density distribution in the (002) plane can be seen, which yields a cross section of the *A*-site electron density. Looking at the cross section of the *A*-site, it is apparent that the *A*-site cations are distributed over different positions as the white arrows point out.

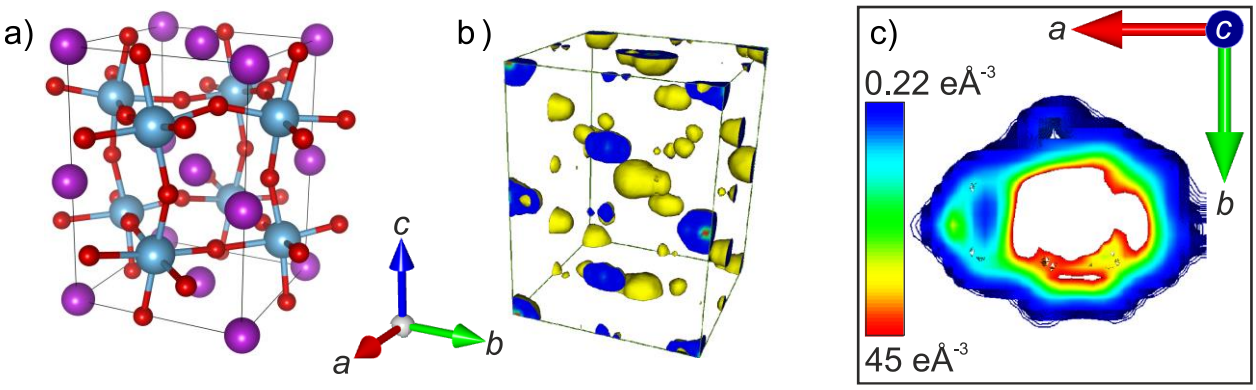

Figure 1. For BTFM–*x*CTO when $x = 0.175$ after the refinement in $Pna2_1$: **a)** initial model where *A*-site cations are represented in purple, *B*-site cations in blue, and oxygens atoms in red, **b)** 3D electron density distribution, and **c)** cross section of the observed electron density distribution for the *A*-site in the (002) plane. The bar at the right bottom shows the electron density, the units are meÅ^{-3}. The values of electron density increase from blue to red.

Figure 2 (top panel) shows that for the initial model (preliminary reference model) the observed and simulated electron density distributions are very different. By analyzing the observed electron density maps, the location of maxima in the *A*-sites was estimated and incorporated into the initial model for the next step of Rietveld refinement. This process of performing a Rietveld analysis and MEM was repeated iteratively, the MEM/Rietveld method, until the reference model and the MEM density were consistent.[63] A detailed description of this building of a disordered structural model for the *A*-site study is explained in the SI. In Figures S23-38, the Rietveld refinements, and the corresponding observed and simulated electron density distribution maps of the *A*-site for the (002) plane for all the structural models are shown. The structural parameters from all these Rietveld refinements are listed in Tables S3-10. In Table S11, for all the different structural models built using the MEM/Rietveld method against SR-PXRD data R_{wp} values, and corresponding figures are listed for comparison. Thus, a six-site disordered model for the *A*-site,

was built based on the electron density distribution for the composition x = 0.175 using the MEM/Rietveld method. Investigation of the 3D observed electron density distribution of the six *A*-site shows overlap of electron density, creating three, elongated pairs of atoms (Bi1-Bi3 are 0.35 Å apart, Bi2-Bi4 are 0.27 Å apart, and Bi5-Bi6 are 0.31 Å apart) seen in Figure S39. Consequently, we considered that this six-site disordered model can also be modelled as three-sites with anisotropic displacement. The initial atomic positions taken for the analysis were the average of each pair of atoms seen in Figure S37. In Figure 2 (bottom panel), we can observe that for the final model the observed and simulated electron density distributions are almost identical. Therefore, a very good fit with an R_{wp} of 1.14% was achieved (Figures S37). Figure 2 shows a schematic summary of this work using the MEM/Rietveld method.

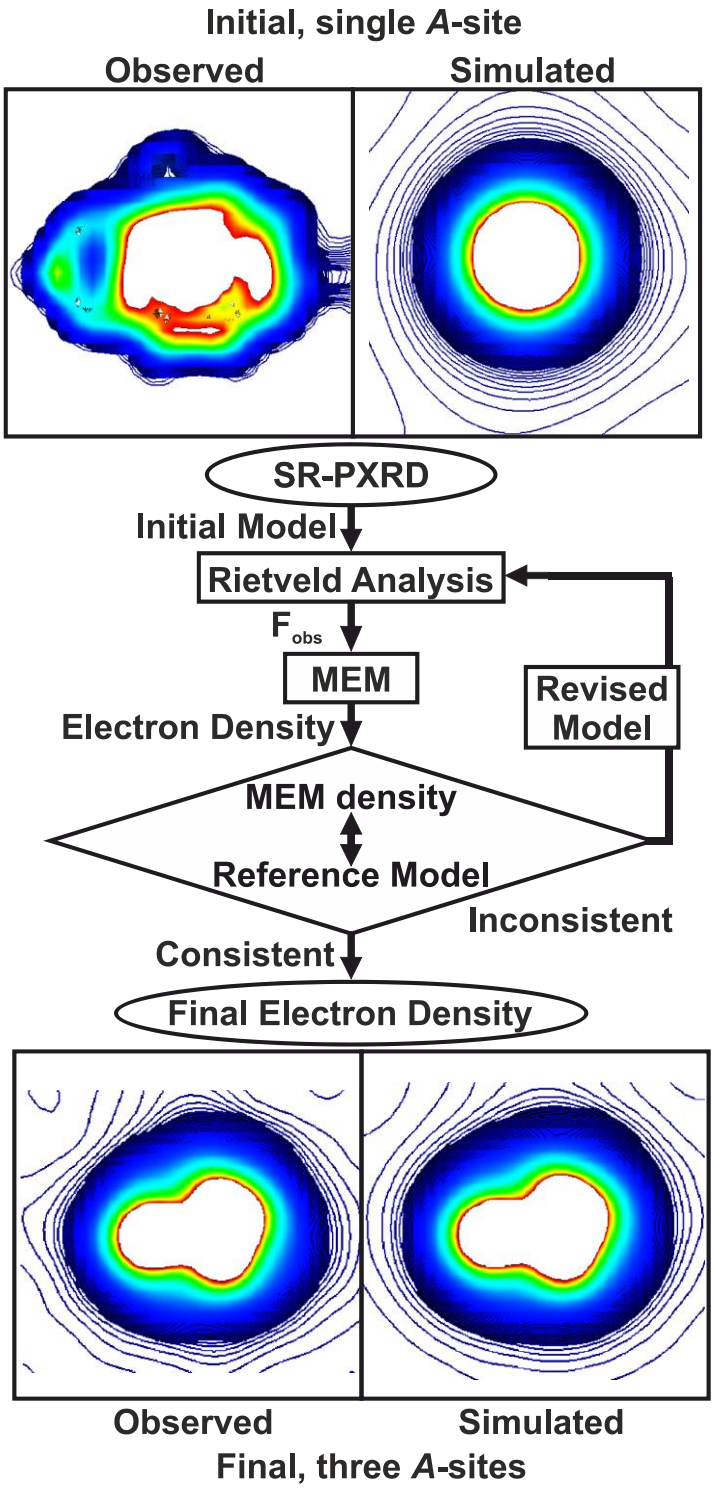

Figure 2. Schematic summary about the building of a structural disordered model for the *A*-site work using the MEM/Rietveld method for BTFM–*x*CTO when x = 0.175 at T = -173 °C.

The $x = 0.175$ composition is very close to the MPB, and when making pellets for physical properties measurements and large samples for neutron diffraction, we noticed tiny amounts of the $R_{[111]}$ phase for some samples (Figure S40). Our MEM and Rietveld analysis shows a pure $O_{[001]}$ phase, but the desire to understand the oxygen sublattice required large samples for neutron diffraction. The synthetic difficulty associated with the removal of all traces of the $R_{[111]}$ phase prompted us to shift our focus to $x = 0.20$ composition. This composition was easily synthesized in large enough sizes for neutron diffraction and sintered into pellets for physical property measurements that showed no trace of a $R_{[111]}$ secondary phase. Complete removal of the $R_{[111]}$ phase ensures that the resultant structural model is entirely from the $O_{[001]}$ phase and that a discussion of contributions from phase coexistence is negated.

3.2.4. Combined Rietveld refinement on x = 0.20. Thus, a combined refinement was performed on $x = 0.20$ at $T = 27$ °C. The three disordered *A*-site model considering anisotropic atomic displacement for the *A*-site previously built by the MEM/Rietveld method was used as starting model. The Rietveld refinement can be seen in Figure 3. The quality of the fit is very good, and an R_{wp} of 5.03% achieved. In Table S12, the structural parameters obtained from this combined refinement are shown. We observe that the value of B_{eq} for O2 is large (3.8 $Å^2$).

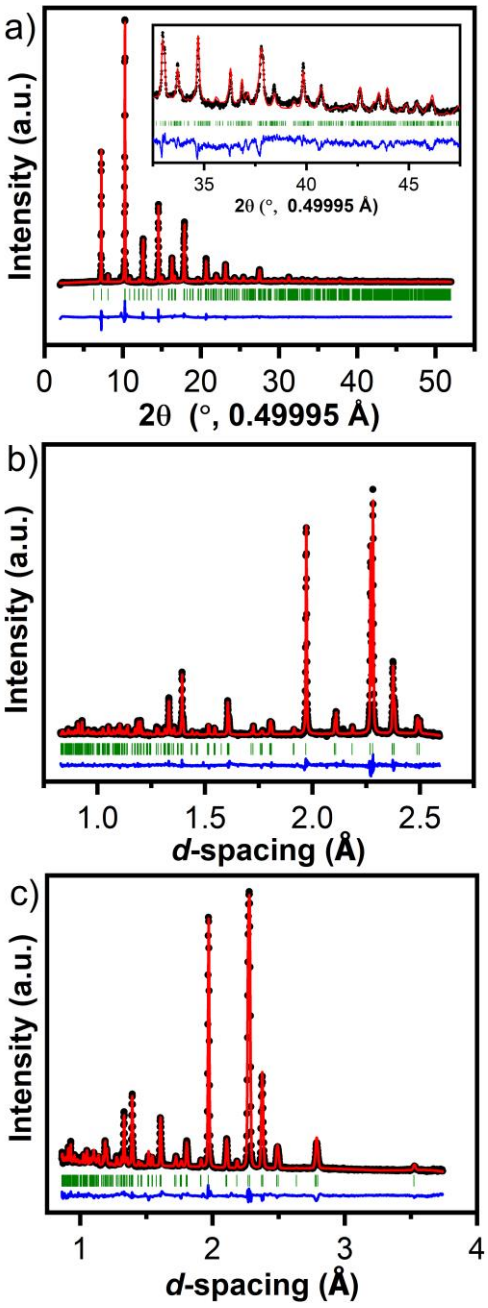

Figure 3. For BTFM–*x*CTO when x = 0.20 results for combined Rietveld refinement on: **a)** SR-PXRD, **b)** Bank 1 of HRPD, and **c)** Bank 2 of HRPD at room temperature in $Pna2_1$ symmetry with the three *A*-site disordered, a single *B*-site, and an unsplit O. The black circles represent the observed data while the red solid line represents the model. The difference blue curve is below. The green tick marks represent positions of Bragg reflections.

To identify the origin of this large B_{eq}, the nuclear density distribution was studied using the NPD data. Looking at the Fourier difference map (Figure S41) reveals the origin of the large B_{eq} for the O2 site. Missing nuclear density is distributed above and below the O2 site along the *c*-axis. This observation led to the splitting of the O2 site into two half occupied oxygen positions. The atomic positions of these sites were constrained together along the *a* and *b*-axis and allowed to displace. The results of this refinement can be seen in Figure 4. This model fits very well visually, reduced the R_{wp} to 4.95%, and yielded a more reasonable value of B_{eq} of 1.8 $Å^2$ for the O2 sites. Attempts to refine the Ca^{2+} and Bi^{3+} occupancies on the three *A*-site, while maintaining the overall composition, gave us negative B_{eq} values for the O1 site, regardless of starting from equally occupied positions, or random distributions. Inclusion of the impurity phases (Aurivillius and Sillénite) reduced the R_{wp} further to 4.80% and did not impact the model because the small quantity of impurities resulted in the only observable peaks being resolved from the main phase. We therefore conclude that the model with equal occupancies of the three *A*-sites and a split O2 site is the most reasonable structural model, and the final one.

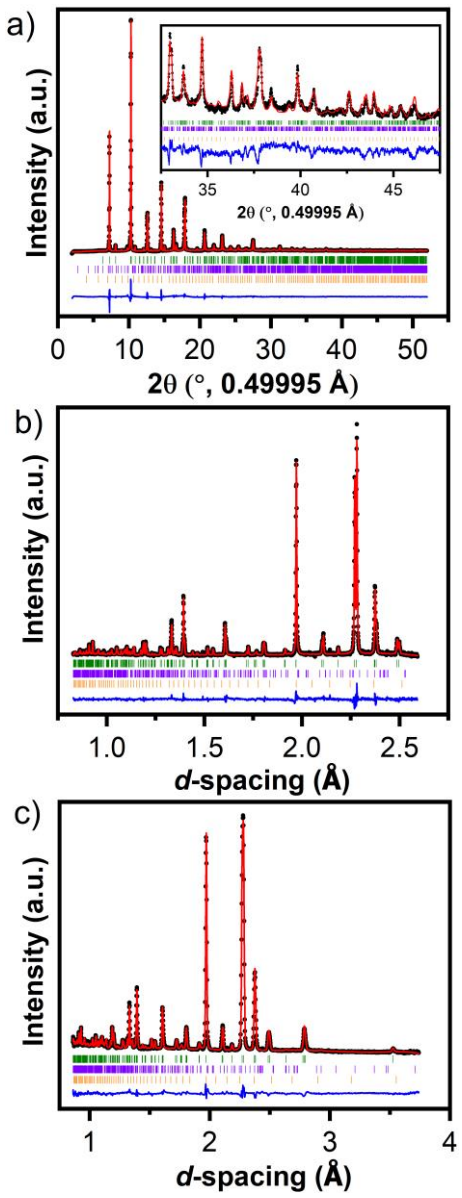

Figure 4. For BTFM–*x*CTO when x = 0.20 results for combined Rietveld refinement on: **a)** SR-PXRD, **b)** Bank 1of HRPD, and **c)** Bank 2 of HRPD at room temperature in $Pna2_1$ symmetry with the three *A*-site disordered, a single *B*-site, and O2 split along the *c*-axis model. The black circles represent the observed data while the red solid line represents the model. The difference blue curve is below. Tick marks indicating *hkl* positions are shown for BTFM–*x*CTO when x = 0.20 (green),

the Aurivillius impurity ($Bi_5Ti_3FeO_{15}$, 0.39(12) mol%, purple), and Sillénite impurity ($Bi_{25}FeO_{40}$, 0.14(6) mol%, orange).

A list of refined values for the model with three disordered *A*-site and two O2 sites is summarized in Table 1, and a list of bond lengths and selected bond angles can be seen in Table S13. The bond lengths are reasonable for a perovskite oxide, even when considering all of the possible cation and oxygen arrangements. In addition to having reasonable bond lengths, the bond valence sums (BVS) (Table S14) are more reasonable for this model compared to others. Both the one and three disordered *A*-site models underestimate the BVS of all cations in the system except Mg^{2+}, which is overestimated. Also, the one *A*-site model overestimates the BVS for Ti^{4+}. This is a marginal improvement in the weighted average of the *A*-site BVS (2.59), which should be 2.80, compared to previous analysis of the BTFM parent compound (2.74).[64] This improvement of *A*-site BVS further supports the validity of this structural model.

Table 1. Structural parameters for BTFM–*x*CTO, $x = 0.20$ from joint Rietveld refinement in $Pna2_1$ using a three sites disordered model for the *A*-site considering anisotropic atomic displacement for the *A*-site and the O2 split along the *c*-axis.

Atom	**Site**	***x***	***y***	***z***	**Atomic displacement parameters**					**Occ**
					U_{11}	U_{22}	U_{33}	$U_{12} = U_{23} = U_{13}$	B_{eq} (Å^2)	
Bi1 / Ca1	4a	0.447(2)	-0.011(3)	0.228(2)	0.0046(8)	0.0228(9)	0.008(2)	0	-	0.267 / 0.067
Bi2 / Ca2	4a	0.5454(6)	0.000(1)	0.248(2)	0.0046(8)	0.0228(9)	0.008(2)	0	-	0.267 / 0.067
Bi3 / Ca3	4a	0.442(2)	0.000(3)	0.283(2)	0.0046(8)	0.0228(9)	0.008(2)	0	-	0.267 / 0.067
Ti / Fe / Mg	4a	-0.022(1)	-0.011(2)	0	-	-	-		0.03(8)	0.50 / 0.20 / 0.30
O1	4a	0.222(1)	0.719(1)	0.050(2)	-	-	-		1.4(1)	1
O2a	4a	0.208(1)	0.713(2)	0.513(1)	-	-	-		1.8(2)	0.5
O2b	4a	0.208(1)	0.713(2)	0.449(1)	-	-	-		1.8(2)	0.5
O3	4a	0.0129(1)	0.0689(2)	0.253(1)	-	-	-		1.29(8)	1

The refined crystal structure and polyhedral environments are shown in Figure 5. The final model has distinct differences from other reported $Pna2_1$ perovskites in regard to lattice parameters and tilt angles. The lattice parameters for $x = 0.20$ fall in between the larger $BiInO_3$ and smaller $CdTiO_3$ structures, but both of these structures have larger tilts of their octahedra: 24.16° along $(100)_p$, 17.21° along $(010)_p$, and 19.41° along $(001)_p$; and 13.76° along $(100)_p$, 17.04° along $(010)_p$, and 15.01° along $(001)_p$, respectively.[11,47] The tilts for $x = 0.20$ are 12.3° along $(100)_p$; 11.7° (O2a) or 15.75 (O2b) along $(010)_p$, and 11.1° along $(001)_p$. These small tilt angles are easily observed in Figures 5a, b, and c. This difference in structures is not surprising as $BiInO_3$ is synthesized at high pressure and has a very small Goldschmidt tolerance factor (*t*) of 0.894, and though $CdTiO_3$ has a

very similar *t* (0.956 versus 0.957 for $x = 0.20$) the reported structure is from a refinement at 4 K. In regards to lattice parameters and tilt angles the structure that $x = 0.20$ most closely resembles is $LaFeO_3$ (LFO) (*Pnma*, $t = 0.954$), though its non-polar space group illustrates some differences.[65] The lattice parameters of LFO differ by less than 0.025 Å, and the tilt angles of 11.48° along $(100)_p$ and $(010)_p$ and 12.05° along $(001)_p$ represent a less than 1° difference, with the exception of the O2b environment which has a 4.27° larger tilt.

The *B*-site octahedral environments can be seen in Figures 5d and e. The displacement of the *B*-site cation from the centroid is obvious, but displacement in the *ab* plane is larger than in along *c*, the polar direction. The displacement along the *c*-axis is on average 0.091 Å, with an entirely O2a polyhedral environment having a displacement of 0.176 Å and the O2b environment having a displacement of 0.005 Å. Though there are two different anion environments, $Pna2_1$ has only one *B*-site cation environment, which is occupied with 50% Ti^{4+}, 20% Fe^{3+}, and 30% Mg^{2+}. There is no sign of cation ordering and no ability to refine cation occupancies within this average structural model. However, a study of the local structure performed by pair distribution function (PDF) analysis and reverse Monte Carlo (RMC) modelling on the BTFM parent showed that Ti^{4+} exists in a different polyhedral environment from Fe^{3+} or Mg^{2+}.[64] For $x = 0.20$, these data cannot identify whether different cation environments exist in the O phase, but the different anion environments observed for a material with 12.5% more Ti^{4+} on the *B*-site gives an indication that this feature seen in the parent has been enhanced.

The most unique structural feature of this perovskite is possibly the *A*-site polyhedral environments, which can be seen in Figures 5f-m. The magnitude of cation displacements from their centroids along different crystallographic directions are summarized in Table S15. In the charge ice pyrochlore $Bi_2Ti_2O_7$, Bi^{3+} is seen displacing in multiple directions which decrease the

Bi-O distance, so the disordering of displacements is consistent with the known behavior of Bi^{3+}.[5] The displacements from the centroid of the polyhedra along the *c*-axis are of particular importance, as it is the polar axis. The *A*1 and *A*2 sites are both displaced in the same $[00\bar{1}]$ direction with displacements of 0.26 and 0.11 Å, respectively. These displacements are in the same direction as the *B*-sites, but are twice the magnitude. The *A*3 site is displaced in the opposite $[001]$ direction by 0.17 Å. All of these sites have equal occupancies, and though the *A*3 site is displaced antipolar to the *A*1 and *A*2 sites, the net *A*-site displacement along the *c*-axis is 0.20 Å in the $[00\bar{1}]$ direction.

The three *A*-sites have approximately the same *y* coordinate, with the *A*1 site having a 0.06 Å (y = -0.011(3)) displacement from y = 0. The atomic displacement parameters for these sites are elongated along this direction (Figure 5a and c). The positions along the *a*-axis are more varied. The *A*1 and *A*3 sites are both displaced towards the origin (x < 0.5) and the *A*2 away from it. The largest displacements are in the *x* direction, with the *A*1 and *A*3 cations showing 0.32 Å and 0.35 Å displacements from the centroid, respectively. The displacements along both the *a*- and *b*-axis ultimately do not contribute to polarization due to the 2_1 screw along the *c*-axis, which generates antiferroelectric correlations in the *ab* plane.

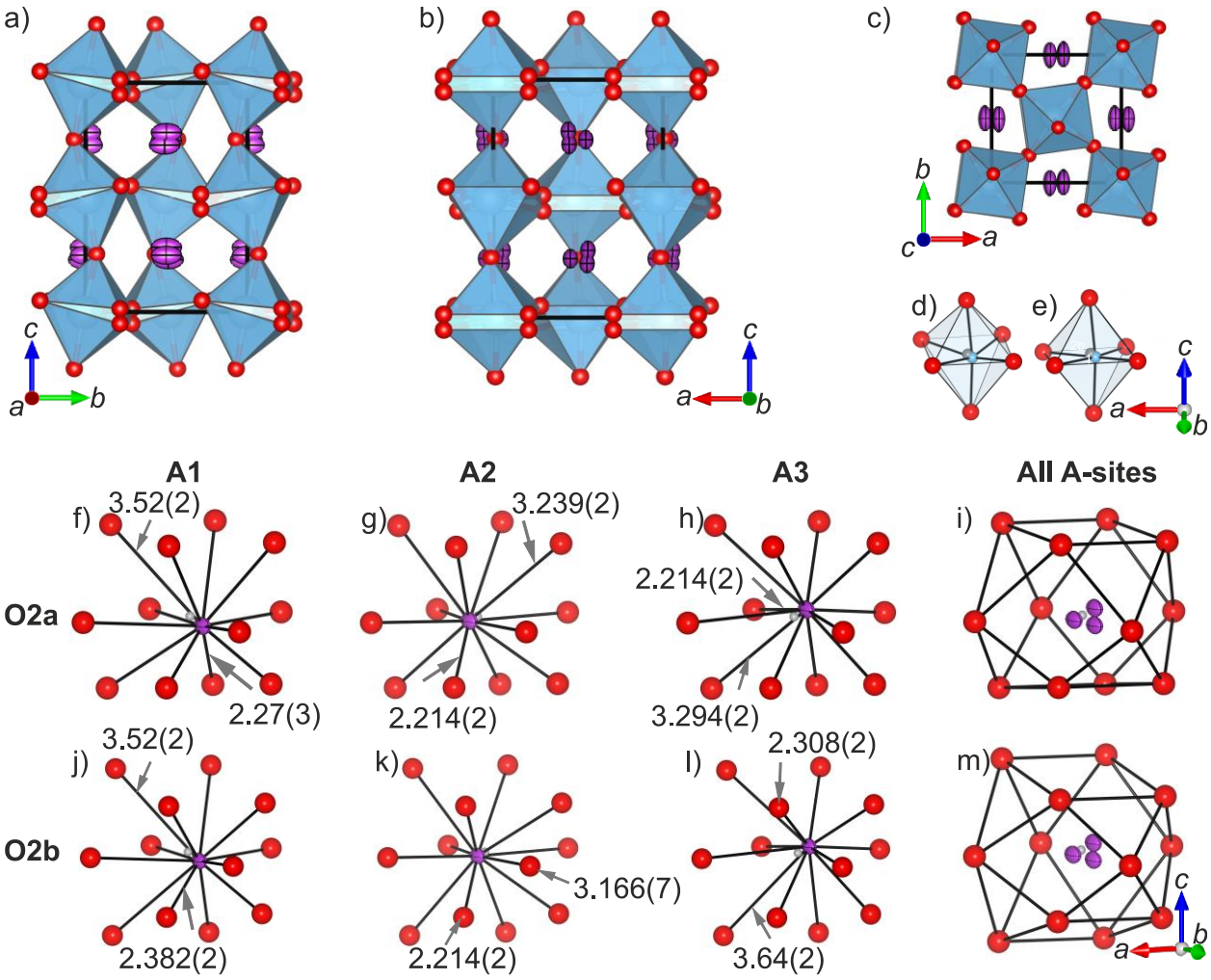

Figure 5. The refined structure for BTFM-*x*CTO when $x = 0.20$. The whole structure can be seen along the **a)** *a*, **b)** *b*, and **c)** *c*-axis. The *B*-site octahedral environments are shown surrounded by **d)** O2a and **e)** O2b oxygens. The permutations of the three *A*-sites with two O2 sites are shown in **f – m)**. The environments for **f)** *A*1, **g)** *A*2, **h)** *A*3, and **i)** all three *A*-site are shown with O2a oxygens, and the environments for **j)** *A*1, **k)** *A*2, **l)** *A*3, and **m)** all three *A*-site are shown with O2b oxygens. The shortest and longest bonds have been labelled. The centroids of polyhedral environments are represented as grey spheres, oxygens are red spheres, *B*-sites are blue spheres, and the *A*-sites are shown as purple thermal ellipsoids.

Looking at these cation displacements together reveals a connection between the $O_{[001]}$ phase and the $R_{[111]}$ phase. Neither the *A*2 or *A*3 sites have displacements along the *b*-axis, and *A*1 has a very small displacement in this direction. The *Pna*2_1 space group has a $\sqrt{2}$ shift of the lattice relative to the cubic aristotype, so displacements with [100] and [001] components (the (010) plane), relative to *Pna*2_1, fall on the $(101)_p$ plane, relative to the cubic cell. If displacements were equal in magnitude along the *a*- and *c*-axis ([100] = [001]), then the displacement vector would be $[111]_p$, or locally rhombohedral. All *A*-sites have displacements primarily along the *a*- and *c*-axis, making the displacements $[uuv]_p$ in nature, and existing in a mirror plane between $[111]_p$ and $[001]_p$. A global polarization vector in the $[uuv]_p$ direction the same as the monoclinic (*Cc*) symmetry, which has been discussed in previous BTFM studies, but with different octahedral rotations.[20,64] Regardless of the observation of local deviations from [001] displacements, any displacements in the *ab* plane are non-polar due to the 2_1 screw along the *c*-axis. The chemical origin of antiferroelectric correlations in the *ab* plane is unclear, but it is reminiscent of the $R_{[111]}$ antiferroelectric nanodomains seen in $NaNbO_3$.[34,66] The ferroelectric cation ordering in $x = 0.20$ is unique and raises more questions about local cation ordering preferences in highly disordered perovskites and its impact on the bulk piezoelectric, ferroelectric, and dielectric properties. Local structural studies using PDF analysis and RMC modelling have been used to study Bi-based pyrochlore oxides[5,61,67] and thermoelectric chalcogenides[6,7] and would unravel the chemical driving force leading to different displacements from the *A*-site centroid.

3.2.5. Variable temperature SR-PXRD analysis on x = 0.20. Le Bail analysis were performed on $x = 0.175$ and 0.20 for the VT SR-PXRD data from -173 to 27 °C in the orthorhombic polar space group *Pna*2_1. The amount of lattice distortion (δ) from the cubic unit cell was calculated using $\delta = (a-b)/(a+b)$. Le Bail fits can be seen in Figures S42 – 46 and S48 – 56 and the refined parameters

can be seen in Table S16 and 17. The lattice parameters evolve linearly as a function of temperature, (Figure S47 and S57) showing no indication of a phase transition.

Le Bail analysis was also performed on VT SR-PXRD data from 27 to 357 °C on $x = 0.20$ (Figures S58 – 69, Table S19). As Figure 6a shows the lattice parameters increase linearly with increasing temperature as expected. In Figure 6b, we can observe that the distortion of the orthorhombic lattice increases with temperature. However, the expectation is that on heating the distortion should decrease.[22] This behavior has been also observed in the materials $Bi_{0.7}Nd_{0.3}FeO_3$ and $Bi_{0.5}La_{0.5}FeO_3$, which both crystallizes in the non-polar space group *Pnma*.[22,23] These linear lattice parameters show no indication of any phase transition through the temperature range investigated. Interestingly, the *a* and *c* lattice parameters change more rapidly, 3.4 and 4.2 fm $°C^{-1}$ respectively, than the *b* lattice parameter (2.3 fm $°C^{-1}$). This more rapid change in lattice parameters may be to do with correlation of displacements seen along these crystallographic directions at room temperature.

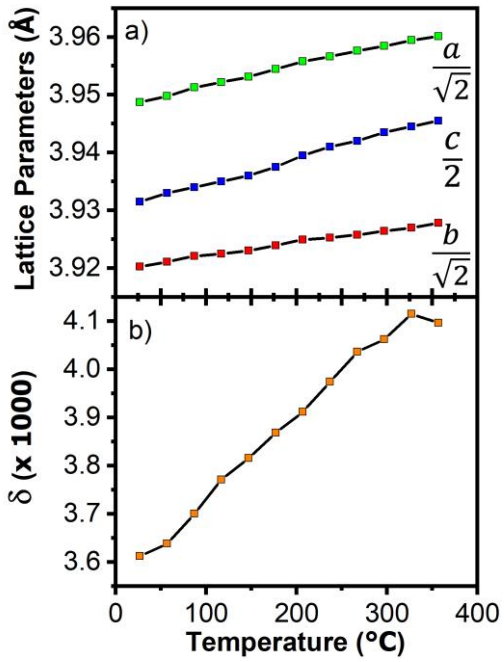

Figure 6. For BTFM-*x*CTO when $x = 0.20$, temperature dependence from 27 to 357 °C of the: **a)** lattice parameters, which have been modified to relate to a cubic perovskite, and **b)** the orthorhombic lattice distortion (δ).

3.3. Physical Properties. *3.3.1. Ferroelectric and Piezoelectric Properties on x = 0.20.* *P*(*E*) loops for $x = 0.20$ were measured at room temperature, seen in Figure 7a. Saturated *P*(*E*) loops were not observed even up to a high field of 150 kV cm^{-1}, and there is no significant remanent polarization. However, the polarization does not evolve linearly with increasing electric field at both 1 and 0.1 Hz (Figure S70), indicative of ferroelectric domain wall motion.[68] Electrical breakdown occurs above an electric field of 150 kV cm^{-1}, and prevents ferroelectric switching at room temperature. Similar behavior has been observed for other related ferroelectrics such as the parent BTFM (*R*3*c*)[20], 0.95BTFM-0.05CTO (*R*3*c*)[26], 0.72BTFM-0.28LFO (*Pmc*2$_1$), and 0.625BTFM-0.25LFO-0.125La(Mg$_{1/2}$Ti$_{1/2}$)O$_3$ (*Pmc*2$_1$).[25] The electromechanical strain was studied at room temperature with a measurement frequency of 1 Hz. The bipolar *S*(*E*) loop (Figure 7b) has a strain response of

0.023%, consistent with the low-field d_{33} value of 2.2 pC N^{-1} previously reported.[1] No negative strain was observed at room temperature (Figure 7b). Interestingly, the strain response does not change linearly with electric field, but with the square indicating that it is dominated by electrostriction.[69,70] The strain response as a function of polarization (Figure S71) cannot be modelled linearly, but is modelled well with a quadratic function, which further demonstrates this electrostrictive character.[70,71] An electrostrictive response is often seen in non-polar materials but is uncommon in polar materials as piezoelectric response is so much larger.[70] The observation of an electrostrictive strain response in a material that has been confirmed to be non-centrosymmetric indicates that the applied field is below the field needed to switch the polarization, known as the coercive field.[72] This illustrates the strong Bi-O bonding interactions (intrinsic response) and that the ferroelectric domains (extrinsic response) are immobile at this applied field.

The coercive field in ferroelectric materials reduces with increasing temperature. Thus, we performed $P(E)$ and $S(E)$ measurements at higher temperature in order to observe the polar properties. At T = 250 °C $S(E)$ loops (Figure 7d) show significant changes from room temperature (Figure 7b) with the data looking typical of a ferroelectric with a characteristic butterfly shape. The negative strain and the butterfly loop confirm ferroelectric switching. The observation of high temperature ferroelectric switching indicates that the material is polar at room temperature, but the coercive field is too large to observe switching of the polarization. The high temperature response represents a five-fold increase in piezoelectric strain (0.103%). The effective piezoelectric coefficient (d_{33}^*) was calculated using $d_{33}^* = S_{max}/E_{max}$, where S_{max} is the strain observed at the maximum field (E_{max}). At T = 250 °C, a d_{33}^* of 68.7 pm V^{-1} is obtained, versus the d_{33}^* of 15.3 pm V^{-1} observed at room temperature. The $P(E)$ response yields less insights, showing a typical loop with lossy behavior (Figure 7c).[73–76]

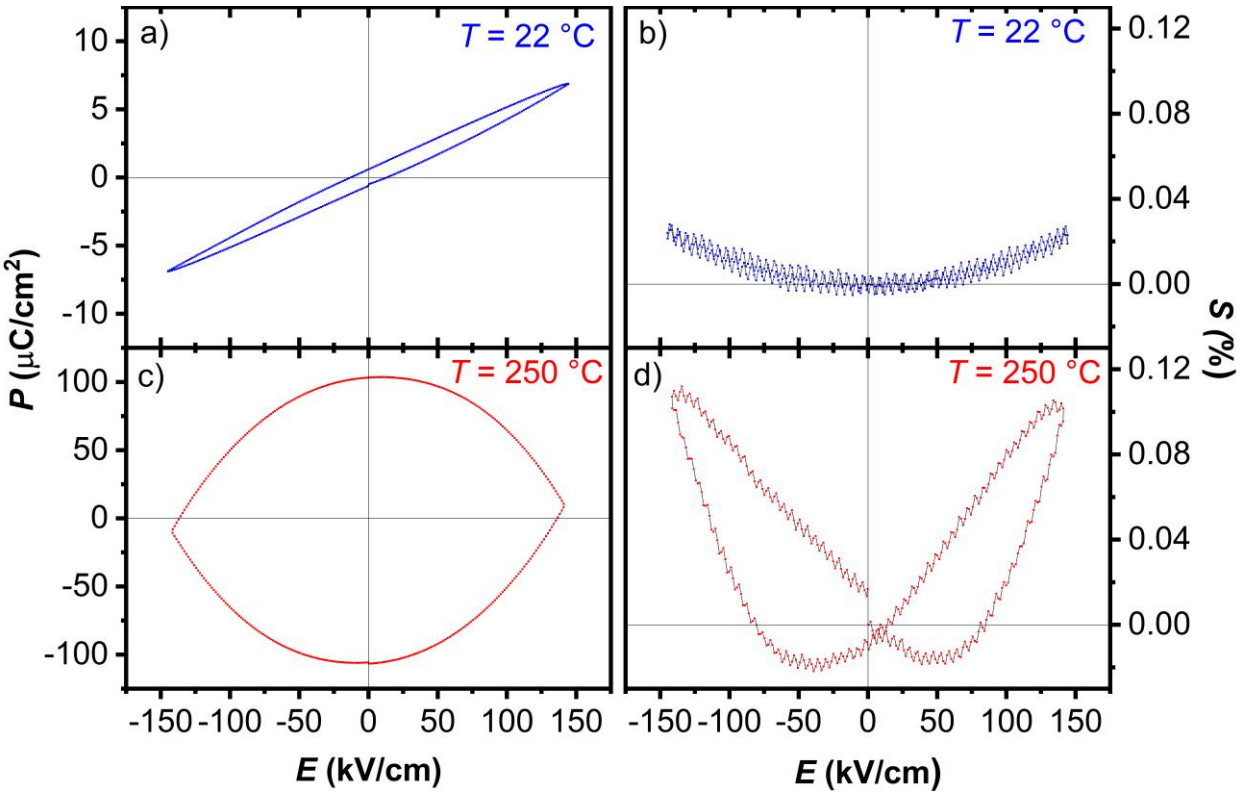

Figure 7. For BTFM– *x*CTO when x = 0.20: $P(E)$ and $S(E)$ loops measured at T = 22 °C (**a**, **b**) and T = 250 °C (**c**, **d**), respectively.

3.3.2. Dielectric Properties on x = 0.20. The dielectric properties were investigated for x = 0.20 from room temperature to T = 360 °C, and the real (ε') and imaginary (ε'') parts of the dielectric permittivity are seen in Figure S70a. The aim of these measurements was to understand better the switching in polarization observed at T = 250 °C. In the temperature range investigated, there is no a sharp feature consistent with a ferroelectric to paraelectric transition, nor an abrupt change in ε', which can be indicative of a ferroelectric to ferroelectric phase transition, such as the *Amm*2 to *P*4*mm* transition in BT.[77] This lack of a phase transition is consistent with our VT SR-XRD analysis. For x = 0.20, the ε' increases to a broad maximum (T_m ~ 170 °C), which is weakly frequency dependent. A broad frequency dependent T_m is indicative of a relaxor material. Relaxor

properties are common in compositionally disordered materials such as NBT-BT.[78] At room temperature and a f = 1kHz, for the unpoled disc of $x = 0.20$ ε' is 492, which is higher than that polar for 0.72BTFM-0.28LFO (~240) [25], and the loss tangent is 0.02.

To determine if the feature seen in the dielectric properties are due to relaxor character, ε' and ε'' were measured on an electrically poled disc (Figure S72b). The poling has no significant difference in the dielectric permittivity, apart from a slight decrease of ε' across the T range measured. There is no peak below T_m which is associated with a depolarization temperature (T_d) or a ferroelectric to relaxor transition ($T_{F\text{-}R}$), which is commonly observed in relaxors.[79–81] This lack of a peak in the poled dielectric data allows us to determine that this is not a relaxor, which is odd for such a heavily disordered material.

3.3.3. Temperature Dependence of the Polarization on x = 0.20. To further investigate the dielectric maximum and the ferroelectric switching, PUND measurements were carried out at different temperatures and the results are shown in Figure S73. When $T < 150$ °C, the switchable polarization value (ΔP) is low and shows minimal change with both temperature and applied electric field. However, when $T > T_m$ (~ 170 °C), the ΔP increases significantly reaching a value of 6 μC cm^{-2} at $T = 200$ °C, which is about 10 times higher than the value observed near room temperature ($\Delta P = 0.57$ μC cm^{-2}). This sudden enhancement of the switchable polarization above T_m explains the $S(E)$ loop distinctive of a butterfly loop obtained at $T = 250$ °C in Figure 7d. The switchable polarization observed on either side of T_m also clearly identifies the presence of ferroelectric contributions from room temperature to 200 °C.

3.4. Structure-property relationships for $x = 0.20$. Understanding the structure property relationships in piezoelectric materials can be challenging due to intrinsic and extrinsic

contributions to the physical properties which must be considered. Despite our structural investigation yielding detailed information on the intrinsic contributions, there are many factors involved. To understand the intrinsic response, the ionic radii, octahedral rotations, chemical bonding preferences, cation displacements, and the correlation of those cation displacements must be discussed.

Perovskites with a high content (>50%) of Bi^{3+} in the *A*-site are complicated to synthesize at ambient pressure because of the small size of Bi^{3+}, which has an ionic radius of 1.36 Å when 12-coordinate. Because the *A*-cation is too small for the 12-coordinate site of the AO_{12} polyhedra, there is a necessity to optimize the anion coordination, and consequently BO_6 octahedra tilt. This is the case with all of the ambient pressure stable pure-Bi *A*-site perovskites, including the polar parent compound BTFM (*R*3*c*, $t = 0.948$) and $x = 0.20$ ($t = 0.952$).[19–21,24] In the case of $PbTiO_3$ (PT), the Pb^{2+} *A*-site has an ionic radius of 1.49 Å. Therefore, no octahedral tilting is observed in the structure and *t* for PT is just above unity ($t = 1.019$). $PbZrO_3$ has octahedral tilting ($t = 0.964$), and in the MPB *t* is just below unity ($t = 0.990 – 0.993$). This structural difference is an obvious differentiation in the chemistry between Bi^{3+} and Pb^{2+} based systems.

BT is another classic ferroelectric perovskite with the same $T_{[001]}$ structure as PT. For the solid solution between BTFM and BT ($t = 1.06$), since the small Bi^{3+} cations are replaced by large Ba^{2+} cations (1.61 Å), at 0.75BTFM-0.25BT ($t = 0.98$) the average tilt angle decreases to zero, resulting in a transition of the space group from *R*3*c* to polar *R*3*m*.[24,82] These symmetries are both $R_{[111]}$, so there is not an MPB with an enhancement in physical properties as expected from a crystal engineering perspective.

A more analogous system to BTFM-*x*CTO is the solid solution between BTFM (t = 0.948) and LFO (t = 0.954), which crystallizes in the same nonpolar orthorhombic space group (*Pnma*) as CTO. In this solid solution the $R_{[111]}$ BTFM parent passes through a polar orthorhombic phase (*Pmc*2$_1$, $O_{[011]}$), for compositions 0.72BTFM-0.28LFO (t = 0.949) and 0.67BTFM-0.33LFO (t = 0.950), before becoming non-polar *Pnma*.[25] In this system the evolution of a structural phase transition is without a significant change in the tolerance factor, as the ionic radius of La^{3+} is the same as for Bi^{3+}. The structural change without changing of t indicates that the difference in preferred bonding environments between La^{3+} and Bi^{3+} drives the change in symmetry.[25] Bismuth and calcium cations also have very similar ionic radius, 1.36 and 1.34 Å respectively. From a cation radii and t perspective the cases of the solid solutions BTFM-*x*LFO, and BTFM-*x*CTO are analogous.

With the increase of content of LFO (*Pnma*) or CTO (*Pnma*), into BTFM (*R*3*c*) the tolerance factor changes minimally. However, phases with polar orthorhombic space groups, subgroups of *Pnma*, are formed with symmetry *Pmc*2$_1$ for BTFM-*x*LFO, and *Pna*2$_1$ in the case of BTFM-*x*CTO. Therefore, a careful consideration of the end members, in terms of ionic radius and tolerance factor, is important to predict the symmetries that could form before attempting to synthesize a new solid solution. From a tolerance factor and crystal chemistry point of view, BTFM-*x*CTO and $Bi_{1-x}La_xFeO_3$ solid solutions are also very similar. As mentioned before, LFO and CTO both have *Pnma* symmetry, and BFO and BTFM both have *R*3*c* symmetry. BTFM-*x*CTO covers a range of tolerance factors from 0.955 to 0.966 as opposed to 0.961 (BFO) to 0.954 (LFO). $Bi_{0.7}La_{0.3}FeO_3$ (0.959) has been reported to have *Pna*2$_1$ symmetry. The *Pna*2$_1$ region in BTFM-*x*CTO is from $0.175 < x < 0.40$, spanning tolerance factors of 0.957 – 0.960.[50] In light of our findings, a closer look at $Bi_{1-x}La_xFeO_3$ around x = 0.30 would be interesting to try to identify

breadth of the *Pna*2_1 region, identify a possible MPB within the solid solution, and better understand the impact that lanthanide substitution has on the local bonding environment in Bi-based ferroelectrics.

For Pb-based systems, it is known that their striking ferroelectric properties are related to the $6s^2$ electronic configuration of Pb^{2+}. The interaction of the s- and p-orbitals of the metal cation with the oxide anion p-states is critical for lone-pair formation resulting in a noncentrosymmetric coordination environment. Studies using *ab initio* calculations to investigate the origin of ferroelectricity for PT and BT indicates that the electronic structure contributes significantly.[83–87] The covalency in the bonding interactions between Pb^{2+} and O ions causes additional polarization, which is absent in predominantly ionic interactions between Ba^{2+} and O in BT. More evidence of polarization of Pb^{2+} at the atomic level was found based on electrostatic potential from SR-PXRD using MEM on PT. The center of the electronic charge density for Pb^{2+} is shifted along the *c*-axis, in agreement with the *ab initio* calculations that the Pb^{2+} and O ion hybridize inducing for the Pb-ion atomic level polarization.[83–88]

Bi-based ferroelectrics rely heavily on the stereochemically active $6s^2$ electronic configuration for their properties. The lack of octahedral tilts makes the PT and BT examples more straightforward, but the bonding interaction of Bi^{3+} and O^{2-} is likely the driving force for the ferroelectric properties observed. It may be that larger piezoelectric strain and ferroelectric polarization in BTFM-*x*CTO is due to the Bi content being higher within the mixed phase region, though the Ti^{4+} content on the *B*-site and the local coordination preference of La^{3+} versus Ca^{2+} are likely contributing factors as well. Regardless of the primary parameter driving the physical properties, the different bonding interaction of Bi^{3+} versus Ca^{2+} cations with O^{2-} anion lattice is certainly the origin of the three *A*-sites observed.

Rietveld refinements found no preference for which site is preferred for which cation. With three *A*-site for two cations the chemistry of each *A*-site is not as obvious. Bond valence sums do not show a clear preference either. The *A*2 site has the smallest displacements off of the centroid and sites *A*1 (Figures 5e and j) and *A*3 (Figures 5h and l) have the largest displacements along the polar *c*-axis. The displacements seen are [*uuv*] in nature, which lies on a mirror plane between the $R_{[111]}$ and $O_{[001]}$ displacements, similar to the monoclinic intermediates facilitating polarization rotation in PZT.[28,34] The ability of *Pna*2_1 symmetry to accommodate these disordered displacements may be the key to the stabilization of the MPB in this system as it would facilitate the phase transition in a continuous instead of discrete manner.

In *Pna*2_1 displacements in the *ab* plane are antiferroelectrically ordered due to the 2_1 screw along the *c*-axis, whereas for *Pnma* symmetry there are antiferroelectric displacements along the *c*-axis as well. In $x = 0.20$, the *A*1 and *A*3 cations are displaced along the *c*-axis but are antiferroelectrically displaced relative to each other along this direction. The coherence length of short-range antiferroelectric ordering along the *c*-axis is not known and would require single crystal diffuse scattering studies. Their existence explains the increase in dielectric permittivity from room temperature (Figure S72) to 360 °C, despite there being no phase transition observed in the lattice parameters (Figure 6a). As the unit cell increases with temperature the coherence length of any local antiferroelectric distortions would reduce, generating more dipoles and a larger permittivity. Additionally, this would explain the reduction in coercive field (Figure 7) and the increased polarization observed from PUND (Figure S73). These local displacements are similar to those revealed in local structural studies using PDF analysis of $NaNbO_3$ which identified nanoscale antiferroelectric twins of $R_{[111]}$ domains.[66] This structural feature is reminiscent of *Pnma* symmetry emerging in the *Pna*2_1 material. The observation of locally disordered [*uuv*]

displacements, bridging *R*3*c* and *Pna*2$_1$, symmetry, combined with the observation of locally disordered antiferroelectric displacements along the *c*-axis, bridging *Pna*2$_1$ and *Pnma* symmetry, highlights structural complexity of this region of the phase diagram and generates further insights into how to stabilize MPBs in octahedrally tilted systems.

These displacements from polyhedral centroids illustrate the large local displacements, which come with large polarization, but the polarization from the cell is calculated to only be 30 μC cm^{-2} (Figure S74, Table S19) due to the previously mentioned antiferroelectric correlations.[89] The low calculated polarization is consistent with the saturation polarization seen in the room temperature P(E) measurements of only 6 μC/cm^2. The lower measured value than calculated is expected for polycrystalline samples versus (001) oriented single crystals. The experimentally observed polarization is in contrast to the MPB (x = 0.075 – 0.1625) compositions which have polarizations of 20 – 50 μC/cm^2.[26] This polarization is much smaller than other Bi based material such as Bi_2ZnTiO_6 (102 μC cm^{-2}) or $Bi_2ZnTi_{0.6}Mn_{0.4}O_6$ (96 μC cm^{-2}).[14,90] The large polarization in $Bi_2ZnTi_{0.6}Mn_{0.4}O_6$ contributes to its low d_{33} = 12 pm/V. The lower overall polarization of x = 0.20 (despite the large local displacements) is likely why its piezoelectric response is almost 6 times that of $Bi_2ZnTi_{0.6}Mn_{0.4}O_6$.

Though the *A*2 site (Figures 5g and k) is the closest to the centroid, it has the shortest bond lengths out of all the polyhedra. Whether the Bi^{3+} predominantly occupies the *A*2, as indicated by shorter bonds and larger orbital overlap, or it occupies the larger *A*1 and *A*3 sites due to its slightly larger ionic radii is not clear. These details about the chemical ordering are key to fully understanding the polarization in this material. The disordered local environment is clearly important to stabilizing the *Pna*2$_1$ phase, but whether the origin of it is the difference in local bonding environments of Bi^{3+} and Ca^{2+} or intermediate range correlations of antiferroelectric

interactions is unknown. Electrostatic potential studies for $x = 0.20$ could help to understand the bonding behavior for this material and make this distinction. This complicated structural problem is the key to better understanding how to stabilize $Pna2_1$ symmetry in perovskite oxides and to understand the thermal evolution of the physical properties observed in $x = 0.20$.

As seen previously in the variable temperature SR-PXRD analysis on $x = 0.20$, Le Bail analysis performed from 27 °C to 357 °C show a linear increase of the lattice parameters as T increases (Figure 6a), as expected. Of note is that the rate of change is greater along the a and c directions, which also have large cation displacements. The δ also increases with T (Figure 6b), although it would be expected that on heating the lattice distortion from the cubic unit cell would decrease.[22] There are not evidences of a structural phase transition based on our analysis of variable temperature SR-PXRD data. These structural results are consistent with the lack of a sharp peak on the dielectric properties over the same temperature range (Figure S72a). The change in octahedral rotations has been shown to impact dielectric properties before in the material $Bi_{0.5}La_{0.5}FeO_3$.[23] The increase in dielectric permittivity and increased switchable polarization seen in PUND are likely due to the change in antiferroelectric interactions along the polar c-axis, but increased piezoelectric strain is difficult to definitively link to the structure on an intrinsic level. The complexity of this material which has variable local displacements, antiferroelectric correlations, and disorder on both A-cation and oxygen sublattices in the average structural model prevents the full understanding of the structural origin and the thermal evolution of the physical properties. The changes observed are likely a mixture of different features expressed at different length scales. The change in local displacements, the correlation of displacements in adjacent unit cells, and octahedral rotations would need to be studied using variable temperature neutron total

scattering and should be considered for the future to further understand the physical properties results.

4. CONCLUSIONS

We have confirmed the symmetry of the polar perovskite $O_{[001]}$ end-member that forms an MPB in the solid solution BTFM-*x*CTO when $x = 0.175$ in the space group $Pna2_1$ using SR-PXRD data based on the reflection conditions. The average structure for the $O_{[001]}$ phase has been studied. A three *A*-site disordered model has been built using the MEM/Rietveld method for $x = 0.175$, which can be used for the other composition $O_{[001]}$ under study $x = 0.20$. Upon investigation of all the cation displacements, we conclude that there is a connection between the $O_{[001]}$ and $R_{[111]}$ in that the observed cation disorder places all *A*-site displacements on a $(011)_p$ mirror plane which bridges these polarization vectors. The physical properties are in agreement with the structure crystallizing in the polar space group $Pna2_1$. At room temperature, the ceramic $x = 0.20$ shows only electrostrictive behavior with a strain of 0.023%. $P(E)$ loops do not reach the coercive field, but non-linearity of the $P(E)$ loops as a function of electric field demonstrates domain wall motion. The ε' at room temperature is 492 at 1 kHz. When the T increases, the coercive field reduces allowing polarization switching. With the barrier to switching overcome the strain increases to 0.103% (d_{33}* = 68.7 pm V^{-1}) at T = 250 °C, obtaining a butterfly loop characteristic of a ferroelectric material. The increase in switched polarization with increasing temperature allows us to track this change. VT SR-PXRD studies and dielectric data show no structural phase transition from room temperature up to 357 °C.

This work highlights the power of the MEM/Rietveld method in helping generate sensible structural models for materials with extreme disorder. The structure of $x = 0.20$ crystallizes in a

very uncommon space group, the *A*-site cation disorder observed is unlike other perovskites in the literature, and the cation disorder observed helps deepen the local structural understanding of the origin of the MPB in BTFM-*x*CTO. The information gained from this average structural model approaches the level of detail of much more complicated analysis, such as RMC. Our results detail a strategy for stabilizing *Pna*2_1 or other polar orthorhombic perovskite oxides using careful consideration of *A*-site cations and tolerance factors. Further study of the structure at the local level using PDF analysis and RMC modelling would deepen the understanding of the mechanism stabilizing this symmetry and causing the MPB right at the boundary between the $O_{[001]}$ phase and the mixed phase region ($O_{[001]}$ + $R_{[111]}$).

ASSOCIATED CONTENT

Supporting Information.

The Supporting Information is available free of charge at...

Compositional analysis details x = 0.175 and 0.20. for Le Bail fits results for BTFM-*x*CTO when x = 0.175 at T = -173 °C using SR-PXRD data in the three polar subgroups of *Pnma*: *Pna*2_1, *Pmc*2_1, and *Pmn*2_1, in the six possible different settings for an orthorhombic structure. Comparison of SR-PXRD data for BTFM-*x*CTO ceramics with orthorhombic structure in the compositional range: $0.175 \leq x \leq 0.400$. Results of the Rietveld refinements of SR-PXRD data for x = 0.175 at room temperature. Construction of the structural model using the MEM-Rietveld method against SR-PXRD. Rietveld analysis of the initial structural model for x = 0.175. Structural information from the joint Rietveld refinement of x = 0.20 in *Pna*2_1 at T = 27 °C using a three sites disordered model

for the *A*-site considering anisotropic atomic displacement for the *A*-site and the O2 split along the *c*-axis (bond lengths, bond angles, bond valence sum, displacements of *A*- and *B*-site cations from oxygen anion centroids). Le Bail fit results for $x = 0.175$ and $x = 0.20$ from variable temperature SR-PXRD data from -173 to 27 °C. Le Bail fit results for $x = 0.20$ from variable temperature SR-PXRD data from 27 to 357 °C. Polarization versus electric field ($P(E)$) measurements on $x = 0.20$ taken at increasing electric fields and different frequencies. Strain (S) response as a function of polarization from $P(E)$ and $S(E)$ data collected at room temperature on $x = 0.20$. Dielectric permittivity against temperature for unpoled and poled discs at the different frequencies for $x = 0.20$. Switched polarization as obtained from the positive-up-negative-down (PUND) measurement at variable temperature for $x = 0.20$. Results of the calculated polarization for $x = 0.20$.

[CCDC 2045200 contains the supplementary crystallographic data for this paper. These data can be obtained free of charge from The Cambridge Crystallographic Data Centre via www.ccdc.cam.ac.uk/data_request/cif.]

AUTHOR INFORMATION

Corresponding Authors

J. B. Claridge - Department of Chemistry, University of Liverpool, Liverpool L69 7ZD, United Kingdom; E-mail: j.b.claridge@liv.ac.uk;

M. J. Rosseinsky - Department of Chemistry, University of Liverpool, Liverpool L69 7ZD, United Kingdom; E-mail: m.j.rosseinsky@liv.ac.uk

Present Addresses

†Neutron Scattering Division, Oak Ridge National Laboratory, Oak Ridge, Tennessee, 37831 United States

[¥] Department of Physics, SRM University – AP, Amaravati, 522502, Andhra Pradesh, India

[¶]Institute of Inorganic Chemistry, RWTH Aachen University, Landoltweg 1, 52056 Aachen, Germany

[§]Department of Physics, Faculty of Pure and Applied Sciences and Tsukuba Research Center for Energy Materials Science, University of Tsukuba, 1-1-1 Tennodai, Tsukuba, Ibaraki 305-8571, Japan

[£]International Center of Synchrotron Radiation Innovation Smart (SRIS), Tohoku University, Katahira 2-1-1, Aoba-ku, Sendai 980-8577, Japan

Author Contributions

The manuscript was written through contributions of all authors. All authors have given approval to the final version of the manuscript.

Notes

The authors declare no competing financial interest

ACKNOWLEDGMENT

The authors thank the European Research Council (ERC Grant agreement 227987 RLUCIM), the European Union (SOPRANO project Grant No. PITN-GA-2008-214040) and the Engineering and Physical Sciences Research Council (EP/H000925) for support. A.M.S., E.N., and M.T. thank RIKEN International Program Associate (IPA) for support and Dr. Kato for experimental help at SPring-8 BL44B2. The synchrotron radiation experiments were performed at BL44B2 in SPring-8 with the approval of RIKEN. The authors wish to express their gratitude to Dr. Aziz Daound-

Aladine at ISIS for the neutron diffraction beamtime at HRPD. This material is based upon work supported by the U.S. Department of Energy, Office of Science, Office of Basic Energy Sciences, under contract number DE-AC05-00OR22725.

REFERENCES

(1) Damjanovic, D.; Klein, N.; Li, J.; Porokhonskyy, V. What Can Be Expected from Lead-Free Piezoelectric Materials? *Funct. Mater. Lett.* **2010**, *3* (1), 5–13.

(2) Bell, A. J.; Deubzer, O. Lead-Free Piezoelectrics - The Environmental and Regulatory Issues. *MRS Bull.* **2018**, *43* (8), 581–587.

(3) Manjón-Sanz, A. M.; Dolgos, M. R. Applications of Piezoelectrics: Old and New. *Chem. Mater.* **2018**, *30* (24), 8718–8726.

(4) Laurita, G.; Puggioni, D.; Hickox-Young, D.; Rondinelli, J. M.; Gaultois, M. W.; Page, K.; Lamontagne, L. K.; Seshadri, R. Uncorrelated Bi Off-Centering and the Insulator-to-Metal Transition in Ruthenium $A_2Ru_2O_7$ Pyrochlores. *Phys. Rev. Mater.* **2019**, *3* (9), 95003.

(5) Shoemaker, D. P.; Seshadri, R.; Tachibana, M.; Hector, A. L. Incoherent Bi Off-Centering in $Bi_2Ti_2O_6O'$ and $Bi_2Ru_2O_6O'$: Insulator versus Metal. *Phys. Rev. B - Condens. Matter Mater. Phys.* **2011**, *84* (6), 064117.

(6) Rathore, E.; Juneja, R.; Culver, S. P.; Minafra, N.; Singh, A. K.; Zeier, W. G.; Biswas, K. Origin of Ultralow Thermal Conductivity in N-Type Cubic Bulk $AgBiS_2$: Soft Ag Vibrations and Local Structural Distortion Induced by the Bi $6s^2$ Lone Pair. *Chem. Mater.* **2019**, *31* (6), 2106–2113.

(7) Bernges, T.; Peilstöcker, J.; Dutta, M.; Ohno, S.; Culver, S. P.; Biswas, K.; Zeier, W. G.

Local Structure and Influence of Sb Substitution on the Structure-Transport Properties in AgBiSe2. *Inorg. Chem.* **2019**, *58* (14), 9236–9245.

(8) Yan, M.; Xue, H. G., Guo, S. P Recent Achievements in Lone-Pair Cation-Based Infrared Second-Order Nonlinear Optical Materials. *Cryst. Growth Des.* **2021**, *36* (5).

(9) Belik, A. A.; Wuernisha, T.; Kamiyama, T.; Mori, K.; Maie, M.; Nagai, T.; Matsui, Y.; Takayama-muromachi, E. High-Pressure Synthesis, Crystal Structures, and Properties of Perovskite-like $BiAlO_3$ and Pyroxene-like $BiGaO_3$. *Chem. Mater.* **2006**, *18* (1), 133–139.

(10) Mangalam, R. V. K.; Bhat, S. V; Iyo, A.; Tanaka, Y.; Sundaresan, A.; Rao, C. N. R. Dielectric Properties, Thermal Decomposition and Related Aspects of $BiAlO_3$. *Solid State Commun.* **2008**, *146*, 435–437.

(11) Belik, A. A.; Stefanovich, S. Y.; Lazoryak, B. I.; Takayama-Muromachi, E. $BiInO_3$: A Polar Oxide with $GdFeO_3$-Type Perovskite Structure. *Chem. Mater.* **2006**, *18* (7), 1964–1968.

(12) Belik, A. A.; Iikubo, S.; Kodama, K.; Igawa, N.; Shamoto, S.; Niitaka, S.; Azuma, M.; Shimakawa, Y.; Takano, M.; Izumi, F.; Takayama-Muromachi, E. Neutron Powder Diffraction Study on the Crystal and Magnetic Structures of $BiCoO_3$. *Chem. Mater.* **2006**, *18* (3), 798–803.

(13) Oka, K.; Azuma, M.; Chen, W.; Yusa, H.; Belik, A. A.; Takayama-muromachi, E.; Mizumaki, M.; Ishimatsu, N.; Hiraoka, N. Pressure-Induced Spin-State Transition in $BiCoO_3$. *J. Am. Ceram. Soc.* **2010**, *132* (6), 9438–9443.

(14) Suchomel, M. R.; Fogg, A. M.; Allix, M.; Niu, H.; Claridge, J. B.; Rosseinsky, M. J. Bi_2ZnTiO_6: A Lead-Free Closed-Shell Polar Perovskite with a Calculated Ionic Polarization

of 150 MCcm^{-2}. *Chem. Mater.* **2006**, *18* (21), 4987–4989.

(15) Market Report: Global Piezoelectric Device Market; Acmite Market Intelligence, 2017, 532.

(16) Piezoelectric Devices Market by Material (Piezoceramics, Piezopolymers, Piezocomposites, Piezocrystals), Prodcuts (Actuators, Transducers, Motors, Sensors, Generators), Applications (Industrial, Automotive, Healthcare, Consumer) — Global Forecast to 2022; MARKETS and MARKETS, 2017, 169.

(17) Bhide, V. G.; Multani, M. S. Mossbauer Effect in Ferroelectric-Antiferromagnetic $BiFeO_3$. *Solid State Commun.* **1965**, *3*, 271–274.

(18) Valant, M.; Axelsson, A. K.; Alford, N. Peculiarities of a Solid-State Synthesis of Multiferroic Polycrystalline $BiFeO_3$. *Chem. Mater.* **2007**, *19* (22), 5431–5436.

(19) Catalan, G.; Scott, J. F. Physics and Applications of Bismuth Ferrite. *Adv. Mater.* **2009**, *21* (24), 2463–2485.

(20) Bridges, C. A.; Allix, M.; Suchomel, M. R.; Kuang, X.; Sterianou, I.; Sinclair, D. C.; Rosseinsky, M. J. A Pure Bismuth a Site Polar Perovskite Synthesized at Ambient Pressure. *Angew. Chemie - Int. Ed.* **2007**, *46* (46), 8785–8789.

(21) Hughes, H.; Allix, M. M. B.; Bridges, C. A.; Claridge, J. B.; Kuang, X.; Niu, H.; Taylor, S.; Song, W.; Rosseinsky, M. J. A Polar Oxide with a Large Magnetization Synthesized at Ambient Pressure. *J. Am. Chem. Soc.* **2005**, *127* (40), 13790–13791.

(22) Kavanagh, C. M.; Lightfoot, P.; Morrison, F. D. Superexchange-Mediated Negative Thermal Expansion in Nd-Doped $BiFeO_3$. *J. Mater. Chem. C* **2018**, *6* (13), 3260–3270.

(23) Kavanagh, C. M.; Goff, R. J.; Daoud-Aladine, A.; Lightfoot, P.; Morrison, F. D. Magnetically Driven Dielectric and Structural Behavior in $Bi_{0.5}La_{0.5}FeO_3$. *Chem. Mater.* **2012**, *24* (23), 4563–4571.

(24) Dolgos, M.; Adem, U.; Wan, X.; Xu, Z.; Bell, A. J.; Comyn, T. P.; Stevenson, T.; Bennett, J.; Claridge, J. B.; Rosseinsky, M. J. Chemical Control of Octahedral Tilting and Off-Axis A Cation Displacement Allows Ferroelectric Switching in a Bismuth-Based Perovskite. *Chem. Sci.* **2012**, *3* (5), 1426–1435.

(25) Dolgos, M. R.; Adem, U.; Manjón-Sanz, A.; Wan, X.; Comyn, T. P.; Stevenson, T.; Bennett, J.; Bell, A. J.; Tran, T. T.; Halasyamani, P. S.; Claridge, J. B.; Rosseinsky, M. J. Perovskite B-Site Compositional Control of $[110]_p$ Polar Displacement Coupling in an Ambient-Pressure-Stable Bismuth-Based Ferroelectric. *Angew. Chemie - Int. Ed.* **2012**, *51* (43), 10770–10775.

(26) Mandal, P.; Manjón-Sanz, A.; Corkett, A. J.; Comyn, T. P.; Dawson, K.; Stevenson, T.; Bennett, J.; Henrichs, L. F.; Bell, A. J.; Nishibori, E.; Takata, M.; Zanella, M.; Dolgos, M. R.; Adem, U.; Wan, X.; Pitcher, M. J.; Romani, S.; Tran, T. T.; Halasyamani, P. S.; Claridge, J. B.; Rosseinsky, M. J. Morphotropic Phase Boundary in the Pb-Free (1-*x*)$BiTi_{3/8}Fe_{2/8}Mg_{3/8}O_3$-*x*$CaTiO_3$ System: Tetragonal Polarization and Enhanced Electromechanical Properties. *Adv. Mater.* **2015**, *27* (18), 2883–2889.

(27) Wu, H.; Zhang, Y.; Wu, J.; Wang, J.; Pennycook, S. J. Microstructural Origins of High Piezoelectric Performance: A Pathway to Practical Lead-Free Materials. *Adv. Funct. Mater.* **2019**, *29* (33), 1–14.

(28) Cox, D. E.; Noheda, B.; Shirane, G. Low-Temperature Phases in $PbZr_{0.52}Ti_{0.48}O_3$: A

Neutron Powder Diffraction Study. *Phys. Rev. B* **2005**, *71* (13), 134110.

(29) Frantti, J. Notes of the Recent Structural Studies on Lead Zirconate Titanate. *J. Phys. Chem. B* **2008**, *112* (21), 6521–6535.

(30) Yokota, H.; Zhang, N.; Taylor, A. E.; Thomas, P. A.; Glazer, A. M. Crystal Structure of the Rhombohedral Phase of $PbZr_{1-x}Ti_xO_3$ Ceramics at Room Temperature. *Phys. Rev. B* **2009**, *80* (10), 1–12.

(31) Zhang, N.; Yokota, H.; Glazer, A. M.; Thomas, P. A. Neutron Powder Diffraction Refinement of $PbZr_{1-x}Ti_xO_3$. *Acta Crystallogr. Sect. B Struct. Sci.* **2011**, *67* (5), 386–398.

(32) Gorfman, S.; Keeble, D. S.; Glazer, A. M.; Long, X.; Xie, Y.; Ye, Z. G.; Collins, S.; Thomas, P. A. High-Resolution x-Ray Diffraction Study of Single Crystals of Lead Zirconate Titanate. *Phys. Rev. B* **2011**, *84* (2), 3–6.

(33) Wang, Y. U. Diffraction Theory of Nanotwin Superlattices with Low Symmetry Phase: Application to Rhombohedral Nanotwins and Monoclinic M_A and M_B Phases. *Phys. Rev. B* **2007**, *76* (2), 1–11.

(34) Noheda, B.; Cox, D. E.; Shirane, G.; Gonzalo, J. A.; Cross, L. E.; Park, S. E. A Monoclinic Ferroelectric Phase in the $Pb(Zr_{1-x}Ti_x)O_3$ Solid Solution. *Appl. Phys. Lett.* **1999**, *74* (14), 2059–2061.

(35) Noheda, B. Structure and High-Piezoelectricity in Lead Oxide Solid Solutions. *Curr. Opin. Solid State Mater. Sci.* **2002**, *6* (1), 27–34.

(36) Zhang, N.; Yokota, H.; Glazer, A. M.; Ren, Z.; Keen, D. A.; Keeble, D. S.; Thomas, P. A.; Ye, Z. G. The Missing Boundary in the Phase Diagram of $PbZr_{1-x}Ti_xO_3$. *Nat. Commun.*

2014, *5*, 1–9.

(37) Zhang, N.; Yokota, H.; Glazer, A. M.; Keen, D. A.; Gorfman, S.; Thomas, P. A.; Ren, W.; Ye, Z. G. Local-Scale Structures across the Morphotropic Phase Boundary in $PbZr_{1-x}Ti_xO_3$. *IUCrJ* **2018**, *5*, 73–81.

(38) Damjanovic, D. Contributions to the Piezoelectric Effect in Ferroelectric Single Crystals and Ceramics. *J. Am. Ceram. Soc.* **2005**, *88* (10), 2663–2676.

(39) Noheda, B.; Cox, D. E. Bridging Phases at the Morphotropic Boundaries of Lead Oxide Solid Solutions. *Phase Transitions* **2006**, *79* (1–2), 5–20.

(40) McQuade, R. R.; Dolgos, M. R. A Review of the Structure-Property Relationships in Lead-Free $(1-x)Na_{0.5}Bi_{0.5}TiO_3$-$(x)BaTiO_3$. *J. Solid State Chem.* **2016**, *242*, 140–147.

(41) Usher, T. M.; Forrester, J. S.; Dela Cruz, C. R.; Jones, J. L. Crystal Structure of $0.96(Na_{0.5}Bi_{0.5}TiO_3)$-$0.04(BaTiO_3)$ from Combined Refinement of X-Ray and Neutron Diffraction Patterns. *Appl. Phys. Lett.* **2012**, *101* (15), 152906.

(42) Kumar, M. M.; Srinivas, A.; Suryanarayana, S. V. Structure Property Relations in $BiFeO_3$ /$BaTiO_3$ Solid Solutions. *J. Appl. Phys.* **2000**, *87* (2), 855–862.

(43) Leontsev, S. O.; Eitel, R. E. Dielectric and Piezoelectric Properties in Mn-Modified $(1-x)BiFeO_3$-$xBaTiO_3$ Ceramics. *J. Am. Ceram. Soc.* **2009**, *92* (12), 2957–2961.

(44) Zhu, J.; Feng, S.; Liu, Q.; Zhang, J.; Xu, H.; Li, Y.; Li, X.; Liu, J.; Huang, Q.; Zhao, Y.; Jin, C. Temperature and Pressure Effects of Multiferroic Bi_2NiTiO_6 Compound. *J. Appl. Phys.* **2013**, *113* (14), 143514.

(45) Sun, P. H.; Nakamura, T.; Shan, Y. J.; Inaguma, Y.; Itoh, M. Study on the Dielectric Property and Structure of Perovskite Titanate $CdTiO_3$. *Ferroelectrics* **1998**, *217* (1), 137–145.

(46) Sasaki, S.; Prewitt, C. T.; Bass, J. D. Orthorhombic Perovskite $CaTiO_3$ and $CdTiO_3$: Structure and Space Group. *Acta Crystalographica* **1987**, *34*, 1668–1674.

(47) Kennedy, B. J.; Zhou, Q.; Avdeev, M. The Ferroelectric Phase of $CdTiO_3$: A Powder Neutron Diffraction Study. *J. Solid State Chem.* **2011**, *184* (11), 2987–2993.

(48) Zhang, H.; Flacau, R.; Sun, J.; Li, G.; Liao, F.; Lin, J. Synthesis, Structure, and Magnetic Properties of $(Tb_{1-x}Mn_y)MnO_{3-\delta}$. *Inorg. Chem.* **2014**, *53* (9), 4535–4540.

(49) Khomchenko, V. A.; Shvartsman, V. V.; Borisov, P.; Kleemann, W.; Kiselev, D. A.; Bdikin, I. K.; Vieira, J. M.; Kholkin, A. L. Effect of Gd Substitution on the Crystal Structure and Multiferroic Properties of $BiFeO_3$. *Acta Mater.* **2009**, *57*, 5137–5145.

(50) Perejón, A.; Sánchez-Jiménez, P. E.; Pérez-Maqueda, L. A.; Criado, J. M.; Romero De Paz, J.; Sáez-Puche, R.; Masó, N.; West, A. R. Single Phase, Electrically Insulating, Multiferroic La-Substituted $BiFeO_3$ Prepared by Mechanosynthesis. *J. Mater. Chem. C* **2014**, *2* (39), 8398–8411.

(51) Kato, K.; Hirose, R.; Takemoto, M.; Ha, S.; Kim, J.; Higuchi, M.; Matsuda, R.; Kitagawa, S.; Takata, M. The RIKEN Materials Science Beamline at SPring-8: Towards Visualization of Electrostatic Interaction. *AIP Conf. Proc.* **2010**, *1234* (2010), 875–878.

(52) Louër, D.; Boultif, A. Powder Pattern Indexing and the Dichotomy Algorithm. *Zeitschrift fur Krist. Suppl.* **2007**, *1* (26), 191–196.

(53) Nishibori, E.; Sunaoshi, E.; Yoshida, A.; Aoyagi, S.; Kato, K.; Takata, M.; Sakata, M. Accurate Structure Factors and Experimental Charge Densities from Synchrotron X-Ray Powder Diffraction Data at SPring-8. *Acta Crystallogr. Sect. A Found. Crystallogr.* **2007**, *63* (1), 43–52.

(54) Sakata, M.; Sato, M. Accurate Structure Analysis by the Maximum-entropy Method. *Acta Crystallogr. Sect. A* **1990**, *46* (4), 263–270.

(55) Tanaka, H.; Takata, M.; Nishibori, E.; Kato, K.; Iishi, T.; Sakata, M. ENIGMA: Maximum-Entropy Method Program Package for Huge Systems. *J. Appl. Crystallogr.* **2002**, *35* (2), 282–286.

(56) Coelho, A. Whole-Profile Structure Solution from Powder Diffraction Data Using Simulated Annealing. *J. Appl. Crystallogr.* **2000**, *33* (3 Part 2), 899–908.

(57) Elliott, C.; Vijayakumar, V.; Zink, W.; Hansen, R. National Instruments LabVIEW: A Programming Environment for Laboratory Automation and Measurement. *J. Assoc. Lab. Autom.* **2007**, *12* (1), 17–24.

(58) Bonneau, P.; Garnier, P.; Husson, E.; Morell, A. Structural Study of PMN Ceramics by X-Ray Diffraction between 297 and 1023 K. *Mater. Res. Bull.* **1989**, *24* (2), 201–206.

(59) Surta, T. W.; Manjón-Sanz, A.; Qian, E.; Tran, T. T.; Dolgos, M. R. Low Temperature Synthesis Route and Structural Characterization of $(Bi_{0.5}A_{0.5})(Sc_{0.5}Nb_{0.5})O_3$ (A = K^+ and Na^+) Perovskites. *Inorg. Chem. Front.* **2018**, *5*, 1033–1044.

(60) Perrin, C.; Menguy, N.; Suard, E.; Muller, C.; Caranoni, C.; Stepanov, A. Neutron Diffraction Study of the Relaxor – Ferroelectric Phase Transition in Disordered

$Pb(Sc_{1/2}Nb_{1/2})O_3$. *J. Phys. Condens. Matter* **2000**, *12*, 7523–7539.

(61) Shoemaker, D. P.; Seshadri, R.; Hector, A. L.; Llobet, A.; Proffen, T.; Fennie, C. J. Atomic Displacements in the Charge Ice Pyrochlore $Bi_2Ti_2O_6O'$ Studied by Neutron Total Scattering. *Phys. Rev. B - Condens. Matter Mater. Phys.* **2010**, *81* (14), 1–9.

(62) Kim, S. J.; Moriyoshi, C.; Kimura, S.; Kuroiwa, Y.; Kato, K.; Takata, M.; Noguchi, Y.; Miyayama, M. Direct Observation of Oxygen Stabilization in Layered Ferroelectric $Bi_{3.25}La_{0.75}Ti_3O_{12}$. *Appl. Phys. Lett.* **2007**, *91* (6), 1–4.

(63) Rietveld, H. M. A Profile Refinement Method for Nuclear and Magnetic Structures. *J. Appl. Crystallogr.* **1969**, *2* (2), 65–71.

(64) Chong, S. Y.; Szczecinski, R. J.; Bridges, C. A.; Tucker, M. G.; Claridge, J. B.; Rosseinsky, M. J. Local Structure of a Pure Bi A Site Polar Perovskite Revealed by Pair Distribution Function Analysis and Reverse Monte Carlo Modeling: Correlated off-Axis Displacements in a Rhombohedral Material. *J. Am. Chem. Soc.* **2012**, *134* (13), 5836–5849.

(65) Dixon, C. A. L.; Kavanagh, C. M.; Knight, K. S.; Kockelmann, W.; Morrison, F. D.; Lightfoot, P. Journal of Solid State Chemistry Thermal Evolution of the Crystal Structure of the Orthorhombic C. *J. Solid State Chem.* **2015**, *230*, 337–342.

(66) Jiang, L.; Mitchell, D. C.; Dmowski, W.; Egami, T. Local Structure of $NaNbO_3$: A Neutron Scattering Study. *Phys. Rev. B* **2013**, *88* (1), 014105.

(67) Daniels, L. M.; Playford, H. Y.; Hannon, A. C.; Walton, R. I. Structural Disorder in (Bi, $M)_2$(Fe, Mn, Bi)$_2O_{6+x}$ (M = Na or K) Pyrochlores Seen from Reverse Monte Carlo Analysis of Neutron Total Scattering. *J. Phys. Chem. C* **2017**, *121* (33), 18120–18128.

(68) Li, S.; Cao, W.; Cross, L. E. The Extrinsic Nature of Nonlinear Behavior Observed in Lead Zirconate Titanate Ferroelectric Ceramic. *J. Appl. Phys.* **1991**, *69* (10), 7219–7224.

(69) Berlincourt, D.; Jaffe, H. Elastic and Piezoelectric Coefficients of Single-Crystal Barium Titanate. *Phys. Rev.* **1958**, *111* (1), 143–148.

(70) Li, F.; Jin, L.; Xu, Z.; Zhang, S. Electrostrictive Effect in Ferroelectrics: An Alternative Approach to Improve Piezoelectricity. *Appl. Phys. Rev.* **2014**, *1*, 011103.

(71) Seifert, K.; Kounga, A. B.; Rödel, J.; Granzow, T.; Jamin, C.; Damjanovic, D.; Zhang, S.-T.; Jo, W. High-Strain Lead-Free Antiferroelectric Electrostrictors. *Adv. Mater.* **2009**, *21* (46), 4716–4720.

(72) Park, S. E.; Wada, S.; Cross, L. E.; Shrout, T. R. Crystallographically Engineered $BaTiO_3$ Single Crystals for High-Performance Piezoelectrics. *J. Appl. Phys.* **1999**, *86* (5), 2746–2750.

(73) Scott, J. F. Ferroelectrics Go Bananas. *J. Phys. Condens. Matter* **2008**, *20* (2), 22–23.

(74) Loidl, A.; Krohns, S.; Hemberger, J.; Lunkenheimer, P. Bananas Go Paraelectric. *J. Phys. Condens. Matter* **2008**, *20* (19), 18–21.

(75) Mahesh Kumar, M.; Palkar, V. R.; Srinivas, K.; Suryanarayana, S. V. Ferroelectricity in a Pure $BiFeO_3$ Ceramic. *Appl. Phys. Lett.* **2000**, *76* (19), 2764–2766.

(76) Maglione, M.; Subramanian, M. A. Dielectric and Polarization Experiments in High Loss Dielectrics: A Word of Caution. *Appl. Phys. Lett.* **2008**, *93* (3), 53–56.

(77) Von Hippel, A. Ferroelectricity, Domain Structure, and Phase Transitions of Barium

Titanate. *Rev. Mod. Phys.* **1950**, *22* (3), 221–237.

(78) Takenaka, T.; Maruyama, K.; Sakata, K. $(Bi_{1/2}Na_{1/2})TiO_3$-$BaTiO_3$ System for Lead-Free Piezoelectric Ceramics. *Jpn. J. Appl. Phys.* **1991**, *30* (9B), 2236–2239.

(79) Anton, E. M.; Jo, W.; Damjanovic, D.; Rodel, J. Determination of Depolarization Temperature of $(Bi_{1/2}Na_{1/2})TiO_3$-Based Lead-Free Piezoceramics. *J. Appl. Phys.* **2011**, *110*, 094108.

(80) Bokov, A. A.; Ye, Z. G. Recent Progress in Relaxor Ferroelectrics with Perovskite Structure. *J. Mater. Sci.* **2006**, *41* (1), 31–52.

(81) McQuade, R.; Rowe, T.; Manjón-Sanz, A.; de la Puente, L.; Dolgos, M. R. An Investigation into Group 13 (Al, Ga, In) Substituted $(Na_{0.5}Bi_{0.5})TiO_3$-$BaTiO_3$ (NBT-BT) Lead-Free Piezoelectrics. *J. Alloys Compd.* **2018**, *762*, 378–388.

(82) Beitollahi, A.; Thomas, N. W. Inter-Relationship of Octahedral Geometry , Polyhedral Volume Ratio and Ferroelectric Properties in Rhombohedral Perovskites. *Acta Crystallogr. Sect. B* **1994**, *B50* (1991), 326–336.

(83) Cohen, R. E.; Krakauer, H. Lattice Dynamics and Origin of Ferroelectricity in $BaTiO_3$: Linearized-Augmented-Plane-Wave Total-Energy Calculations. *Phys. Rev. B* **1990**, *42* (10), 6416–6423.

(84) Cohen, R. E. Origin of Ferroelectricity in Perovskite Oxides. *Nature* **1992**, *358* (6382), 136–138.

(85) Zhong, W.; King-Smith, R. D.; Vanderbilt, D. Giant LO-TO Splittings in Perovskite Ferroelectrics. *Phys. Rev. Lett.* **1994**, *72* (22), 3618–3621.

(86) Zhong, W.; Vanderbilt, D.; Rabe, K. M. First-Principles Theory of Ferroelectric Phase Transitions for Perovskites: The Case of $BaTiO_3$. *Phys. Rev. B* **1995**, *52* (9), 6301–6312.

(87) King-Smith, R. D.; Vanderbilt, D. Theory of Polarization of Crystalline Solids. *Phys. Rev. B* **1993**, *47* (3), 1651–1654.

(88) Tanaka, H.; Kuroiwa, Y.; Takata, M. Electrostatic Potential of Ferroelectric PbTiO3 : Visualized Electron Polarization of Pb Ion. *Phys. Rev. B* **2006**, *74*, 172105.

(89) Capillas, C.; Tasci, E. S.; De La Flor, G.; Orobengoa, D.; Perez-Mato, J. M.; Aroyo, M. I. A New Computer Tool at the Bilbao Crystallographic Server to Detect and Characterize Pseudosymmetry. *Zeitschrift fur Krist.* **2011**, *226* (2), 186–196.

(90) Yu, R.; Matsuda, N.; Tominaga, K.; Shimizu, K.; Hojo, H.; Sakai, Y.; Yamamoto, H.; Oka, K.; Azuma, M. High-Temperature Monoclinic Cc Phase with Reduced c/a Ratio in Bi-Based Perovskite Compound $Bi_2ZnTi_{1-x}Mn_xO_6$. *Inorg. Chem.* **2016**, *55* (12), 6124–6129.

Table of Contents graphic